J. Fluid Mech. (2000), *vol.* 423, *pp.* 33–69. Printed in the United Kingdom

Breaking of axisymmetry and onset of unsteadiness in the wake of a sphere

By BRĂDUŢ GHIDERSA† AND JAN DUŠEK‡

Institut de Mécanique des Fluides de Strasbourg,
2, rue Boussingault, 67000 Strasbourg, France

(Received 20 October 1999 and in revised form 9 March 2000)

The primary and secondary instabilities of the sphere wake are investigated from the viewpoint of nonlinear dynamical systems theory. For the primary bifurcation, a theory of axisymmetry breaking by a regular bifurcation is given. The azimuthal spectral modes are shown to coincide with nonlinear modes of the instability, which provides a good reason for using the azimuthal expansion as an optimal spectral method. Thorough numerical testing of the implemented spectral–spectral-element discretization allows corroboration of existing data concerning the primary and secondary thresholds and gives their error estimates. The ideal axisymmetry of the numerical method makes it possible to confirm the theoretical conclusion concerning the arbitrariness of selection of the symmetry plane that arises. Investigation of computed azimuthal modes yields a simple explanation of the origin of the so-called bifid wake and shows at each Reynolds number the coexistence of a simple wake and a bifid wake zone of the steady non-axisymmetric regime. At the onset of the secondary instability, basic linear and nonlinear characteristics including the normalized Landau constant are given. The periodic regime is described as a limit cycle and the power of the time Fourier expansion is illustrated by reproducing experimental r.m.s. fluctuation charts of the streamwise velocity with only the fundamental and second harmonic modes. Each time–azimuthal mode is shown to behave like a propagating wave having a specific spatial signature. Their asymptotic, far-wake, phase velocities are the same but the waves keep a fingerprint of their passing through the near-wake region. The non-dimensionalized asymptotic phase velocity is close to that of an infinite cylinder wake. A reduced-accuracy discretization is shown to allow qualitatively satisfactory unsteady simulations at extremely low cost.

1. Introduction

The purpose of the present paper is to investigate the instabilities representing the first stages of transition to turbulence of the sphere wake. From the experimental viewpoint the basic difficulty in investigating the transitional Reynolds numbers is a non-intrusive attachment of the sphere. The earliest experiments were carried out with falling objects: liquid drops (Magarvey & Bishop 1961*b*), discs (Willmarth, Hawk & Harvey 1964) and spheres (Magarvey & MacLatchy 1965). In Goldburg & Florsheim (1966) a set of axisymmetric bodies (sphere, cones, discs, teardrops) glide along a wire, which leaves the shedding frequency unaltered but causes an aperiodicity of the

† Present address: Forschungszentrum Karlsruhe, Institut für Reaktorsicherheit, Postfach 3640, D-76021, Karlsruhe, Germany.
‡ Author to whom correspondence should be addressed: e-mail: dusek@imf.u-strasbg.fr

vortex shedding. Achenbach (1974) and Sakamoto & Haniu (1990) attach the rear of a sphere to a sting placed in the flow direction. Ormières (1999) uses a variety of attachments with wires and differently oriented fine capillary tubes and states that there is a significant dependence of the measurements on the perturbations introduced by the attachments. These difficulties explain the sometimes considerable quantitative discrepancies of experimental results. Nevertheless, there is a complete qualitative consensus concerning the scenario of transition in the interval of Reynolds numbers approximately between 150 and about 350.

The flow, which is axisymmetric at low Reynolds numbers, remains steady but becomes asymmetric at a critical Reynolds number Re_1 estimated, experimentally, to lie between 150 (Provansal & Ormières 1997*a*; Ormières 1999) and 190 (Nakamura 1976). The steady asymmetric state is stable until the onset of non-stationarity reported at $Re_2 = 290$ by Magarvey & Bishop (1961*a*) and at $Re_2 = 300$ by Magarvey & MacLatchy (1965) and Sakamoto & Haniu (1990, 1995). Provansal & Ormières (1997*a*) succeeded in determining this critical Reynolds number very precisely as $Re_2 = 273$. The most striking feature of this regime is the double thread (bifid) wake setting in slightly above Re_1. This phenomenon is clearly shown in all experiments using dye injection at the sphere surface. It appears that the dye, instead of being concentrated in just one thread in the wake, is concentrated in two parallel threads. The early observations of Magarvey & Bishop (1961*a*) lead to a classification (Levi 1980) amounting to identifying the wake splitting with the axisymmetry breaking. Nakamura (1976) and Provansal & Ormières (1997*a*) confirm that, actually, axisymmetry breaking (the shift of the single thread wake with respect to the flow axis) is observed at lower Reynolds numbers than the splitting into two threads. Flow visualizations of the steady asymmetric regime show that axisymmetry has been replaced by a plane symmetry.

Unlike in the cylinder wake, the plane symmetry is conserved by the unsteady wake above the non-stationarity threshold. This striking feature can, again, already be seen in Magarvey & Bishop's (1961*b*) visualizations and is confirmed by Achenbach (1974), Sakamoto & Haniu (1990), Provansal & Ormières (1997*b*, 1998) and Ormières (1999). The non-stationarity is very similar to von Kármán vortex shedding in the cylinder wake and is characterized by a typical limit cycle spectrum of the flow velocity fluctuations (Ormières & Provansal 1999). At the onset of instability the unsteadiness is observable as a mere undulation of the two threads of dye of the bifid wake described above. As its amplitude increases, the wake threads form hairpin vortices classified as a new regime by Levi (1980). Most authors attempted to establish the dependence of the Strouhal or Roshko number characterizing the vortex shedding frequency as a function of the Reynolds number and the reported relations allow comparison of the measured Strouhal number for a given Reynolds number value. The discrepancies in the measured vortex shedding frequencies are quite significant. At $Re = 300$ Magarvey & Bishop (1991*b*) give $St \approx 0.1$, Sakamoto & Haniu (1990) $St \approx 0.15$ and Ormières shows that depending on the experimental setup the Strouhal number may vary between 0.07 and 0.137.

The subsequent scenario of transition is much less clear. At $Re = 420$ Sakamoto & Haniu (1990) report 'irregularities' of the vortex shedding, which might be related to the onset of a lower frequency observed by Ormières at $Re = 390$. Above these Reynolds number values the symmetry plane of the wake seems to start to rotate. At $Re \approx 800$ Kelvin–Helmholtz-like 'vortex tubes' are seen by Sakamoto & Haniu (1990) to be shed in the near wake and a high frequency appears in the, already turbulent, spectrum (Ormières 1999).

Numerical work concerning the sphere wake has been limited for a long time to axisymmetric computations unable to capture the loss of axisymmetry.

The need to carry out fully three-dimensional simulations to capture the sphere wake instability focused attention on the linear analysis, which promised to be computationally less demanding. The parallel flow theory fails to provide quantitatively reliable predictions for wakes (Dušek, Fraunié & Le Gal 1994*a*). The viscous parallel linear analysis of Monkewitz (1988) allows, nonetheless, a prediction that the mode with azimuthal wavenumber $m = 1$ (helical mode) is more unstable than the axisymmetric mode for a smooth transverse velocity profile, whereas the converse occurs for velocity profiles approaching the top-hat one. This situation is similar to that of jets (see Michalke 1984) for which a close qualitative relation between parallel theory predictions and fully three-dimensional simulations (Dănăilă, Dušek & Anselmet 1997) has been confirmed. In this qualitative sense it can be said that the theoretical results of Monkewitz (1988) agree well with experimental observations. For the infinite cylinder wake, the availability of accurate two-dimensional unsteady simulations made the fully two-dimensional linear instability analysis of Jackson (1987) an exception, in spite of the great theoretical importance of accurate linear analysis data. For a sphere, Kim & Pearlstein (1990) present a fully two-dimensional (axisymmetric) linear stability analysis by computing the least-stable eigenmodes of the linearized Navier–Stokes operator discretized by a pseudo-spectral method. Their result illustrates the importance of the numerical accuracy of the analysis. It considerably under-predicts the critical Reynolds number (175.1) and, more seriously, yields a complex eigenvalue as the most unstable. A similar method was used by Natarajan & Acrivos (1993) but, this time, with a sufficient accuracy. The linear stability analysis of Natarajan & Acrivos (1993) predicts, for a sphere, a regular primary bifurcation at $Re = 210$ which is in perfect agreement with the experimental observation that the wake loses its symmetry before becoming unsteady. The secondary (Hopf-type) bifurcation develops, in reality, from an asymmetric base flow generated by the primary instability. Nevertheless, it is of interest that the next eigenvalue is predicted to be complex, and to cross the imaginary axis at $Re = 277.5$. Its imaginary part corresponds to a Strouhal number of 0.113, both values being close to those which characterize the actual secondary instability.

The first unsteady and fully three-dimensional direct numerical simulations were presented by Tomboulides, Orszag & Karniadakis (1993). The numerical method used for the simulation is particularly appropriate and accurate. It combines a spectral element decomposition in the axial-radial plane with a spectral expansion along the azimuthal direction. Unfortunately, the potential of the simulation was not fully exploited in the paper. Tomboulides *et al.* (1993) show that their numerical code is able to provide reliable direct numerical simulations up to $Re = 1000$ and test its accuracy by giving several physically important values. They find a critical Reynolds number for axisymmetry breaking at $Re = 212$ and observe an onset of vortex shedding between $Re = 250$ and 285. At $Re = 300$ their Strouhal number is equal to 0.136.

Johnson & Patel (1999) implement a finite difference discretization on a three-dimensional mesh with spherical topology using a dual time stepping for simulation of unsteady flow. The method provides a very good accuracy for resolving finely the spatial structures of the flow but is rather costly for unsteady simulations. The investigated Reynolds number range lies between 50 and 300. The simulations are compared to flow visualizations in a towing tank at the same Reynolds numbers. For the domain in which instabilities occur, Johnson & Patel (1999) find a critical

Reynolds number for axisymmetry breaking $Re_1 = 210$. Above this threshold, the flow is found to be steady and to have only a planar symmetry, the symmetry plane being fixed due to an imperfectly rotationally invariant azimuthal discretization. In the steady asymmetric regime, between the regular and the Hopf bifurcation, only the flow at $Re = 250$ is presented. Streamlines representing (in this steady regime) particle traces simulate the convection of dye in an experimental setup and show the presence of the bifid wake. Three-dimensional plots of vorticity allow the wake threads to be associated to counter-rotating vortical structures. The onset of unsteadiness is located in the interval $Re_2 \in [270, 280]$. The basic problem of computing long histories and taking into account many Reynolds number values is the high computing costs of one Strouhal period (24 hours). The results presented thus concern only $Re = 300$. The flow is shown to keep its plane symmetry in the unsteady regime. Attention is concentrated on the near wake and the vortex shedding from the sphere surface.

Mittal (1999*a*) uses a formulation in spheroidal coordinates to simulate, more generally, an ellipsoidal geometry. For a sphere, the coordinates are spherical and the discretization is based on a Fourier expansion in the azimuthal and polar angle and a Chebyshev collocation in the radial direction. Mittal (1999*b*) pushes the simulations beyond the periodical regime and finds a loss of planar symmetry at $Re < 400$.

To sum up, past investigations prove clearly that the sphere wake passes from steadiness and axisymmetry to unsteadiness in two stages. First it undergoes a regular bifurcation keeping the steadiness and breaking the axisymmetry. In this process an arbitrary symmetry plane is selected. Next, the steady but already non-axisymmetric flow becomes unsteady via a Hopf bifurcation conserving the plane symmetry. Certain questions and problems remain, however, open.

First of all, there is the practical issue of the optimal numerical method of solving the Navier–Stokes equations for the sphere wake. In this paper, we claim that the spectral azimuthal expansion is optimal because it is directly linked to the nonlinear instability theory. Various discretizations in the radial-axial plane might be satisfactory. From our experience with spectral element discretization (Patera 1984) that proved able to resolve very different spatial scales both accurately and efficiently, we retain an analogous approach to Tomboulides *et al.* (1993). We submit the spectral element discretization to a thorough optimization based on testing the mesh independence of the axisymmetry-breaking threshold Re_1. Next we show, by varying the number of azimuthal modes, that in the investigated Reynolds number domain very accurate results can be obtained with an extremely limited number of modes. A weakly nonlinear analysis provides a straightforward explanation of this fact.

Our numerical implementation allows us to carry out both a linear analysis and a fully nonlinear simulation. This, together, with easy control of the discretization accuracy, allows us to determine the primary instability threshold accurately at low cost. Limited computing costs of unsteady simulations provide the possibility of investigating long transients. As a result, we can determine with a similar accuracy the threshold of the secondary (Hopf-type) instability and fit the constants of the Landau model to its transients. A series of previous papers (Dušek, Le Gal & Fraunié 1994*b*; Dušek 1996; Carte, Dušek & Fraunié 1996; Zielinska *et al.* 1997; Dauchy, Dušek & Fraunié 1997) proved the usefulness of a detailed linear, weakly and fully nonlinear analysis of the flow behaviour from the bifurcation theory viewpoint. For the sphere wake an exhaustive theoretical, fully nonlinear, analysis of the bifurcations arising is still missing.

The symmetry-breaking process observed at the primary bifurcation in the sphere wake is in itself an interesting theoretical issue. In a recent paper (Dănăilă, Dušek &

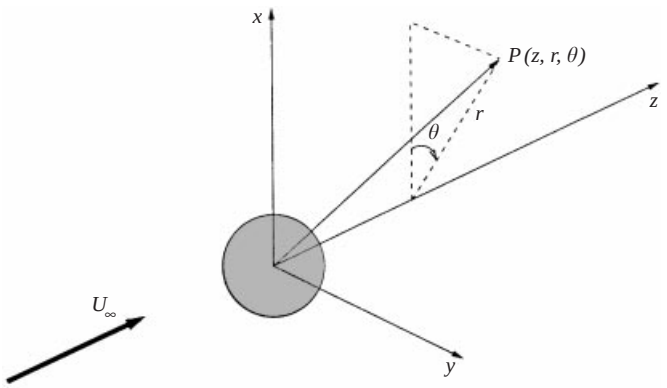

FIGURE 1. Problem geometry. $\boldsymbol{U}_\infty$ is the inflow velocity and the z-axis points in the flow direction.

Anselmet 1998) a scenario expected for axisymmetry breaking at a Hopf bifurcation has been described and theoretically analysed. In the present case of the sphere wake, it has been shown that axisymmetry breaks before a Hopf bifurcation sets in. In this paper, we present a simple proof that in this case the axisymmetry necessarily gives way to a plane symmetry, the plane being arbitrary. Its orientation is selected by initial conditions in perfectly rotationally symmetric configurations or is sensitive to the slightest perturbation of the rotational invariance. A similar proof of the plane-symmetry conservation at the secondary instability is also given.

The existence of one-thread and two-thread wakes in the steady regime has been intriguing many authors involved with the sphere wake. In spite of that, to our knowledge no satisfactory explanation, except the attempt of Levi (1980), has been proposed. The present paper provides a very simple analysis showing that the phenomenon is explainable in terms of growth of the amplitude of the symmetry-breaking unstable mode proportionally to the square root of the instability parameter $(Re - Re_1)/Re_1$.

The previous numerical investigations tend to lead to the false conclusion that even only qualitatively correct simulations require considerable computing resources. We point out that the low-dimensionality of the dynamical system represented by the wake due to the relative weakness of nonlinear effects in the regimes considered allows us to implement qualitatively and quantitatively correct simulations at costs exceeding only by a small factor those of the axisymmetric case.

These issues are treated in the following order: In § 2 we present a theory of axisymmetry breaking relevant to axisymmetric body wakes. In § 3 the numerical method is described. The tests of the mesh and estimates of the accuracy achieved are discussed in § 4. In § 5 the steady asymmetric flow is analysed. Section 6 presents the onset of non-stationarity and analyses the unsteady flow in terms of a double time–azimuthal Fourier expansion.

2. Nonlinear theory of axisymmetry breaking

Let us consider the incompressible Navier–Stokes equations in cylindrical coordinates r, z and θ, the z-axis having its origin in the centre of the sphere and being parallel to the asymptotic flow direction $\boldsymbol{U}_\infty$, r being the distance to the z-axis and θ being the azimuthal angle (see figure 1). If u, v and w represent, respectively, the axial, radial and azimuthal velocity components the Navier–Stokes equations non-

dimensionalized with respect to the inflow velocity U_∞ and the sphere diameter d are as follows:

$$\frac{\partial u}{\partial t}+u\frac{\partial u}{\partial z}+v\frac{\partial u}{\partial r}+\frac{w}{r}\frac{\partial u}{\partial \theta}=-\frac{\partial p}{\partial z}+\nu\left\{\frac{\partial^2 u}{\partial z^2}+\frac{1}{r}\frac{\partial}{\partial r}\left(r\frac{\partial u}{\partial r}\right)+\frac{1}{r^2}\frac{\partial^2 u}{\partial \theta^2}\right\}, \tag{2.1a}$$

$$\frac{\partial v}{\partial t}+u\frac{\partial v}{\partial z}+v\frac{\partial v}{\partial r}+\frac{w}{r}\frac{\partial v}{\partial \theta}-\frac{w^2}{r} =-\frac{\partial p}{\partial r}+\nu\left\{\frac{\partial^2 v}{\partial z^2}+\frac{1}{r}\frac{\partial}{\partial r}\left(r\frac{\partial v}{\partial r}\right)+\frac{1}{r^2}\frac{\partial^2 v}{\partial \theta^2}-\frac{v}{r^2}-\frac{2}{r^2}\frac{\partial w}{\partial \theta}\right\}, \tag{2.1b}$$

$$\frac{\partial w}{\partial t}+u\frac{\partial w}{\partial z}+v\frac{\partial w}{\partial r}+\frac{w}{r}\frac{\partial w}{\partial \theta}+\frac{wv}{r} =-\frac{\partial p}{r\partial \theta}+\nu\left\{\frac{\partial^2 u}{\partial z^2}+\frac{1}{r}\frac{\partial}{\partial r}\left(r\frac{\partial w}{\partial r}\right)+\frac{1}{r^2}\frac{\partial^2 w}{\partial \theta^2}-\frac{w}{r^2}+\frac{2}{r^2}\frac{\partial v}{\partial \theta}\right\}, \tag{2.1c}$$

$$\frac{\partial u}{\partial z}+\frac{1}{r}\frac{\partial}{\partial r}(rv)+\frac{1}{r}\frac{\partial w}{\partial \theta}=0, \tag{2.1d}$$

where ν is the inverse of the Reynolds number $\nu = 1/Re$. To abbreviate the notation we shall introduce the column array $\boldsymbol{v} \equiv (u, v, w)^T$.

For axisymmetric flows the flow field satisfying (2.1) is independent of θ; moreover, for non-swirling flows, there is no azimuthal velocity. The linear stability of an axisymmetric solution $(\boldsymbol{V}, P)$, ($\boldsymbol{V} \equiv (V_z, V_r, V_\theta)^T$ being the axisymmetric velocity field and P the pressure), consists in studying a perturbed flow field

$$\boldsymbol{v} = \boldsymbol{V} + \boldsymbol{v}', \quad p = P + p', \tag{2.2}$$

with an infinitesimal perturbation $\boldsymbol{v}', p'$ expressed via complex eigenmodes $\boldsymbol{\Phi}, \Pi$:

$$\boldsymbol{v}' = \alpha e^{\lambda t}\boldsymbol{\Phi} + \text{c.c.}, \quad p' = \alpha e^{\lambda t}\Pi + \text{c.c.} \tag{2.3}$$

α being a small, but arbitrary, complex constant (c.c. standing for complex conjugate). The perturbation is amplified or dampened depending on the solution of the eigenvalue problem:

$$\lambda\boldsymbol{\Phi} + \mathscr{L}[\boldsymbol{V}]\boldsymbol{\Phi} + \nabla\Pi = 0, \tag{2.4a}$$

$$\nabla\cdot\boldsymbol{\Phi} = 0, \tag{2.4b}$$

where $\mathscr{L}[\boldsymbol{V}]$ is given by

$$\mathscr{L}[\boldsymbol{V}] = \begin{bmatrix} V_z\frac{\partial}{\partial z}+V_r\frac{\partial}{\partial r}+V_\theta\frac{\partial}{r\partial\theta}+\frac{\partial V_z}{\partial z}-\nu\nabla^2, & \frac{\partial V_z}{\partial r}, & 0 \\ \frac{\partial V_r}{\partial z}, & V_z\frac{\partial}{\partial z}+V_r\frac{\partial}{\partial r}+V_\theta\frac{\partial}{r\partial\theta}+\frac{\partial V_r}{\partial r}-\nu\left(\nabla^2-\frac{1}{r^2}\right), & -\frac{2V_\theta}{r}+\frac{2\nu}{r^2}\frac{\partial}{\partial\theta} \\ \frac{\partial V_\theta}{\partial z}, & \frac{\partial V_\theta}{\partial r}+\frac{V_\theta}{r}-\frac{2\nu}{r^2}\frac{\partial}{\partial\theta}, & V_z\frac{\partial}{\partial z}+V_r\frac{\partial}{\partial r}+V_\theta\frac{\partial}{r\partial\theta}+\frac{V_r}{r}-\nu\left(\nabla^2-\frac{1}{r^2}\right) \end{bmatrix} \tag{2.5}$$

with

$$\nabla^2 = \frac{\partial^2}{\partial z^2}+\frac{1}{r}\frac{\partial}{\partial r}r\frac{\partial}{\partial r}+\frac{1}{r^2}\frac{\partial^2}{\partial\theta^2}. \tag{2.6}$$

Owing to the independence of the base flow $\boldsymbol{V}$ of the azimuthal coordinate θ the linear operator $\mathscr{L}[\boldsymbol{V}]$ commutes with $\partial/\partial\theta$, the rotation operator with respect to the flow axis. The common eigenfunctions of both operators thus have the following form:

$$\boldsymbol{\Phi}(z,r,\theta) = \boldsymbol{\sigma}(m)\,\phi_m(z,r)\,\mathrm{e}^{-\mathrm{i}m\theta}, \tag{2.7a}$$

$$\Pi(z,r,\theta) = \pi_m(z,r)\,\mathrm{e}^{-\mathrm{i}m\theta}, \tag{2.7b}$$

where $\boldsymbol{\sigma}(m)$ is the diagonal 3×3 matrix

$$\boldsymbol{\sigma}(m) = \begin{bmatrix} 1 & 0 & 0 \\ 0 & 1 & 0 \\ 0 & 0 & -\mathrm{i}\ \mathrm{sgn}(m) \end{bmatrix}, \tag{2.8}$$

m stands for the azimuthal wavenumber, $m = 0, \pm 1, \pm 2, \ldots$ and the array $\phi_m(z,r) \equiv (\phi_{m,z}, \phi_{m,r}, \phi_{m,\theta})$ represents, respectively, the azimuthal modes of the axial, radial and azimuthal velocity. The sign function $\mathrm{sgn}(m)$ is zero for $m = 0$.

In the general case of rotationally invariant swirling flows ($V_\theta(z,r) \neq 0$) the eigenvalue problem (2.4) breaks up into a sequence of independent eigenvalue problems in m-subspaces:

$$\lambda\phi_m + \Lambda_m[\boldsymbol{V}]\phi_m + \nabla_{|m|}\pi_m = 0, \tag{2.9a}$$

$$\nabla_{|m|}\cdot\phi_m = 0, \tag{2.9b}$$

where

$$\Lambda_m[\boldsymbol{V}] = \begin{bmatrix} V_z\dfrac{\partial}{\partial z} + V_r\dfrac{\partial}{\partial r} - \dfrac{\mathrm{i}m}{r}V_\theta + \dfrac{\partial V_z}{\partial z} - \nu\nabla^2_{|m|}, & \dfrac{\partial V_z}{\partial r}, & 0 \\ \dfrac{\partial V_r}{\partial z}, & V_z\dfrac{\partial}{\partial z} + V_r\dfrac{\partial}{\partial r} - \dfrac{\mathrm{i}m}{r}V_\theta + \dfrac{\partial V_r}{\partial r} - \nu\left(\nabla^2 - \dfrac{1}{r^2}\right), & \dfrac{2V_\theta}{r}\mathrm{i}\,\mathrm{sgn}(m) + \dfrac{2\nu|m|}{r^2} \\ \mathrm{i}\,\mathrm{sgn}(m)\dfrac{\partial V_\theta}{\partial z}, & \mathrm{i}\,\mathrm{sgn}(m)\left(\dfrac{\partial V_\theta}{\partial r} + \dfrac{V_\theta}{r}\right) + \dfrac{2\nu|m|}{r^2}, & V_z\dfrac{\partial}{\partial z} + V_r\dfrac{\partial}{\partial r} - \dfrac{\mathrm{i}m}{r}V_\theta + \dfrac{V_r}{r} - \nu\left(\nabla^2_{|m|} - \dfrac{1}{r^2}\right) \end{bmatrix}, \tag{2.10}$$

$$\nabla_{|m|} = \left(\frac{\partial}{\partial z}, \frac{\partial}{\partial r}, \frac{|m|}{r}\right)^T, \tag{2.11}$$

$$\nabla_{|m|}\cdot = \left[\frac{\partial}{\partial z}, \quad \frac{1}{r}\frac{\partial}{\partial r}r, \quad -\frac{|m|}{r}\right] \tag{2.12}$$

and

$$\nabla^2_{m^2} = \frac{\partial^2}{\partial z^2} + \frac{1}{r}\frac{\partial}{\partial r}\left(r\frac{\partial}{\partial r}\right) - \frac{m^2}{r^2}. \tag{2.13}$$

The eigenvalues $\lambda = \lambda_m$ depend obviously on m. The primary instability corresponds to the first eigenvalue λ_m crossing the imaginary axis.

In the absence of swirl $V_\theta = 0$, the linear operator (2.10) is clearly independent of the sign of m so that

$$\Lambda_m[\boldsymbol{V}] = \Lambda_{|m|}[\boldsymbol{V}], \quad \lambda_m = \lambda_{|m|}, \quad \phi_m = \phi_{|m|}, \quad \pi_m = \pi_{|m|}. \tag{2.14}$$

	$m = 0$	$m \neq 0$
$\mathrm{Im}(\lambda) = 0$	Steady axisymmetric	Steady non-axisymmetric
$\mathrm{Im}(\lambda) \neq 0$	Unsteady axisymmetric	Unsteady non-axisymmetric

TABLE 1. Characteristics of the perturbed flow depending on the azimuthal wavenumber and on the imaginary part of the first eigenvalue to become unstable.

Depending on the azimuthal wavenumber and on the imaginary part of the first eigenvalue to become unstable, the perturbed flow is given in table 1. Natarajan & Acrivos (1993) showed that it is the steady non-axisymmetric case with $m = \pm 1$ which applies to the sphere wake at the primary instability. For λ real, the corresponding eigensolution of (2.9*b*) can be taken real ($\phi_{-m} = \overline{\phi}_m$). For the normalization of the eigenmode, a convenient way is to set the maximum of the absolute value of its radial component equal to 1 (§ 5). Let us denote β the argument of the complex number α representing the amplitude of the initial perturbation amplitude. The flow perturbation that arises then has the form

$$\boldsymbol{v}' = 2|\alpha|\, \mathrm{e}^{\lambda_1 t}\, [\phi_{1,z}(r,z)\cos(\theta-\beta), \phi_{1,r}(r,z)\cos(\theta-\beta), \phi_{1,\theta}(r,z)\sin(\theta-\beta)]^T, \tag{2.15a}$$

$$p' = 2|\alpha|\, \mathrm{e}^{\lambda_1 t}\, \pi_1(r,z)\cos(\theta-\beta). \tag{2.15b}$$

Equations (2.15) together with (2.7*a*) show that the perturbation is symmetric with respect to the plane $\theta = \beta$ chosen arbitrarily by the initial conditions (by the initial perturbation of the flow).

The nonlinear terms of the Navier–Stokes equations (2.1) will generate higher-order harmonics to the fundamental azimuthal mode $\boldsymbol{\Phi}_1$. The perturbation will then be expanded into a full Fourier series:

$$\boldsymbol{v}'(z,r,\theta) = \sum_{m=-\infty}^{\infty} \sigma(m)\, \boldsymbol{v}'_m(z,r)\, \mathrm{e}^{-\mathrm{i}m\theta}, \tag{2.16a}$$

$$p' = \sum_{m=-\infty}^{\infty} p'_m(z,r)\, \mathrm{e}^{-\mathrm{i}m\theta}. \tag{2.16b}$$

(Note that $m = 0$ does not correspond to the whole axisymmetric mode but only to the axisymmetric nonlinear correction of the base flow $\boldsymbol{V}$). When inserted into (2.1) the expansion (2.16) yields the following system of coupled equations:

$$\frac{\partial \boldsymbol{v}'_m}{\partial t} + \Lambda_{|m|}[\boldsymbol{V}]\boldsymbol{v}'_m + \nabla_{|m|} p'_m + \sum_{\ell=-\infty}^{\infty} B_{\ell,m-\ell}(\boldsymbol{v}'_\ell, \boldsymbol{v}'_{m-\ell}) = 0, \tag{2.17a}$$

$$\nabla_{|m|} \cdot \boldsymbol{v}'_m = 0, \tag{2.17b}$$

where

$$B_{\ell,k}(\boldsymbol{v}'_\ell, \boldsymbol{v}'_k) = (\sigma(\ell)\, \boldsymbol{v}'_\ell \cdot \nabla_k)\sigma^{-1}(\ell+k)\sigma(k)\boldsymbol{v}'_k \tag{2.18}$$

and

$$\nabla_k = \left(\frac{\partial}{\partial z},\ \frac{\partial}{\partial r},\ -\mathrm{i}\frac{k}{r}\right)^T. \tag{2.19}$$

To describe the amplification of an infinitesimal perturbation proportional to the real

linear mode we shall assume the initial condition

$$\boldsymbol{v}'_1|_{t=0} = \alpha\,\phi_1, \quad p_1|_{t=0} = \alpha\,\pi_1 \tag{2.20}$$

with a very small complex constant $\alpha = a\,\mathrm{e}^{\mathrm{i}\beta}$.

It is now possible to prove two assertions:

(i) The fully nonlinear perturbation (2.16) is symmetric with respect to the same plane $\theta = \beta$ as the linear one.

(ii) The series (2.16) converges with a convergence rate proportional to the magnitude of the fundamental mode $\boldsymbol{v}_1, p_1$.

To prove the plane symmetry, let us measure the azimuthal angle with respect to the plane selected by the infinitesimal perturbation ($\theta - \beta \to \theta$). Assuming the existence and unicity of the solution of (2.17), (2.20), an assumption confirmed numerically by the successful implementation of the algorithm described in the next section, it is sufficient to prove that a sequence of real modes $\boldsymbol{v}_m, p_m$ satisfies the system for all time t. The series (2.16) will then reduce to a series of cosines for the pressure and the axial and radial velocity components and a series of sines for the azimuthal velocity component. To see this, let us take the complex conjugate of the system. The operators $\Lambda_{|m|}, \nabla_{|m|}$ and $\nabla_{|m|}\cdot$ being manifestly real, it remains to see if the same holds for the nonlinear operator (2.18). It is easily seen that

$$\boldsymbol{\sigma}(\ell + k)^{-1}\boldsymbol{\sigma}(k) = \mathrm{diag}\,(1, 1, \mathrm{sgn}\,(k)\mathrm{sgn}\,(\ell + k)) \tag{2.21}$$

and, written in more detail,

$$\boldsymbol{\sigma}(\ell)\,\boldsymbol{v}'_\ell \cdot \nabla_k = u'_\ell \frac{\partial}{\partial z} + v'_\ell \frac{\partial}{\partial r} - k\,\mathrm{sgn}\,(\ell)\,w'_\ell \frac{\partial}{\partial \theta}. \tag{2.22}$$

As a result, if the sequence of modes $\{\boldsymbol{v}'_m\}$ is a solution, its complex conjugate is solution too and a real solution exists.

To characterize the amplitude of the instability, let us introduce the complex amplitude $A(t)$ using the projection of the fundamental azimuthal mode $(\boldsymbol{v}'_1, p'_1)$ onto the unstable eigenmode (ϕ_1, π_1)

$$\mathrm{Proj}_{(\phi_1,\pi_1)}(\boldsymbol{v}'_1, p'_1) = A(t)\,\mathrm{e}^{-\mathrm{i}\theta}(\sigma(1)\phi_1, \pi_1). \tag{2.23}$$

When very small (for $t \to 0$) $\boldsymbol{v}'_1 \approx A(t)\,\mathrm{e}^{-\mathrm{i}\theta}\,\sigma(1)\,\phi_1 + \mathrm{c.c.}$, but as the amplitude increases, nonlinearities generate other harmonics and deform the fundamental mode. This can be interpreted as higher-order effects of an analytic expansion in $\tilde{A}(t) = A(t)\mathrm{e}^{-\mathrm{i}\theta}$ and $\overline{\tilde{A}(t)} = \overline{A(t)}\mathrm{e}^{\mathrm{i}\theta}$ with a non-zero convergence radius ρ:

$$\boldsymbol{v}'(z, r, \theta; t) = \sum_{\substack{k,\ell \geqslant 0 \\ k+\ell \geqslant 1}} \beta_{k,\ell}(z, r)\tilde{A}^k \overline{\tilde{A}}^\ell \tag{2.24}$$

where $\beta_{k,\ell}$ are some vectorial coefficients. A similar scalar expansion can be assumed to hold for the pressure perturbation. Letting A to be very small, we find $\beta_{1,0} = \sigma(1)\phi_1$. To yield a real sum, the coefficients $\beta_{k,\ell}$ have to satisfy the symmetry relation $\overline{\beta_{k,\ell}} = \beta_{\ell,k}$. A simple rearrangement of the series (2.24) leads to the expansion

$$\boldsymbol{v}'(z, r, \theta; t) = |A|^2 \left(\sum_{k=0}^{\infty} \beta_{k,k}|A|^{2k} \right) + \left[\sum_{m=1}^{\infty} \left(\sum_{k=0}^{\infty} \beta_{m+k,k}|A|^{2k} \right) A^m \mathrm{e}^{-\mathrm{i}m\theta} + \mathrm{c.c.} \right] \tag{2.25}$$

allowing the conclusion that (compare to the Fourier series (2.16))

$$\boldsymbol{v}'_m = A^m \left(\sum_{k=0}^{\infty} \beta_{m+k,k} |A|^{2k} \right), \quad m > 0, \tag{2.26}$$

$$\boldsymbol{v}'_0 = |A|^2 \left(\sum_{k=0}^{\infty} \beta_{k,k} |A|^{2k} \right). \tag{2.27}$$

This means that the m-azimuthal mode (for $|m| > 0$) is of the order of $|A|^{|m|}$ and the axisymmetric correction of the order of $|A|^2$. The series following the leading factors are series of $|A|^2$. Equations (2.26), (2.27) show that, as long as $|A|$ remains within the convergence radius, the Fourier series (2.16) converge and, close to the instability threshold when the nonlinear effects are weak, they can be expected to converge very rapidly.

Being closely linked to the nonlinear theory of axisymmetry breaking in wakes of axisymmetric bodies, the azimuthal Fourier expansion can thus be considered as an optimal discretization for physical reasons. In the present context this may sound trivial because the fundamental azimuthal wavenumber happens to be $m = 1$ and the expansion coincides with the intuitively obvious azimuthal Fourier series. The optimality consists in the theoretical confirmation of the right choice of the fundamental wavenumber and in the proof that the azimuthal modes coincide with nonlinear instability modes, which provides a rapid convergence rate, so rapid that some important phenomena can be analysed with only two modes with a good accuracy.

To end this section we shall briefly discuss a weakly nonlinear characterization of the regular bifurcation analysed above. As mentioned in the introduction, a weakly nonlinear expansion of the Navier–Stokes equations allowed Dušek *et al.* (1994*b*) to obtain the Landau model as a third-order approximation describing the evolution of the fundamental mode of an instability arising from a Hopf bifurcation. Truncating (2.16) to the third order of $|A|$ in expansions (2.26), (2.27) yields, in an analogous manner, a Landau-like equation for the amplitude A:

$$\frac{\mathrm{d}A}{\mathrm{d}t} = \lambda - C|A|^2 A. \tag{2.28}$$

The basic difference with the Landau model of a Hopf bifurcation is that λ is a real eigenvalue and C is a real constant. The latter property is a consequence of the existence of a real solution A as proved above. Equation (2.28) represents a normal form of an axisymmetry-breaking regular bifurcation and can be considered as a generalization of the normal form of a pitchfork bifurcation (see e.g. Strogatz 1994) corresponding to a purely real A. The bifurcation is supercritical if $C > 0$. In that case, (2.28) perfectly illustrates (see figure 2) the arbitrary choice of the phase of the new state corresponding to $|A|^2 = \sqrt{\lambda/C}$. Assuming λ to be proportional to the instability parameter $\epsilon = (Re - Re_{crit})/Re_{crit}$ close to the instability threshold, we find, in the same way as for a pitchfork bifurcation, that the amplitude $|A|$ is proportional to $\sqrt{\epsilon}$.

3. Numerical method

The theoretical considerations of the previous section lead us to conclude that the nonlinear axisymmetry-breaking instability expansion coincides with spectral

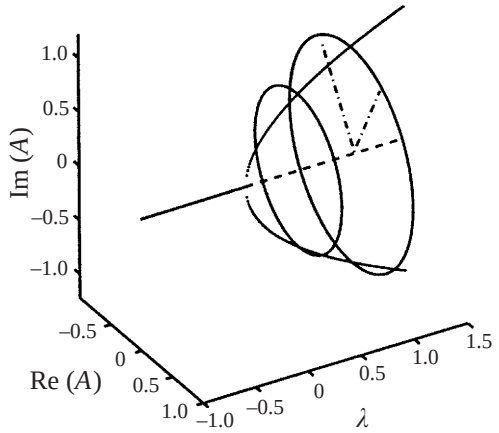

FIGURE 2. Bifurcation diagram of axisymmetry breaking representing the normal form (2.28). Unlike for a Hopf bifurcation diagram, the circles at $\lambda = 0.5$ and $\lambda = 1$ represent two sets of fixed points and not limit cycles. Any point of the set can be selected and is fixed. Two examples of possible trajectories of the system leaving the unstable fixed point $A = 0$ and selecting a stable fixed point $|A|^2 = \lambda/C$ are represented by dash–dotted lines.

Fourier discretization in the azimuthal direction characterized by the fundamental wavenumber $m = 1$. For this reason we retained a spectral–spectral-element space discretization analogous to that of Tomboulides *et al.* (1993) combining the Fourier expansion in the azimuthal direction with a spectral-element discretization in the (z, r)-plane.

In our approach, the method allows both a linear analysis and a fully nonlinear simulation with a small but variable number of azimuthal modes and the nonlinear terms are treated in the spectral space. The purpose of the present section is to summarize the numerical implementation used in the paper, leaving the details to the Appendix § A.1.

The underlying governing equations (2.1) are expanded in the azimuthal direction (θ). Unlike (2.16) we change slightly the notation of the azimuthal modes from now on. The $m = 0$ mode will contain the unperturbed basic flow so that

$$\boldsymbol{v}(z,r,\theta,t) = \sum_{m=-\infty}^{\infty} \boldsymbol{\sigma}(m)\, \boldsymbol{v}_m(z,r,t)\, \mathrm{e}^{-\mathrm{i}m\theta}, \quad p(z,r,\theta,t) = \sum_{m=-\infty}^{\infty} p_m(z,r,t)\, \mathrm{e}^{-\mathrm{i}m\theta}, \tag{3.1}$$

where $\boldsymbol{v}_m = (u'_m, v'_m, w'_m)^T$, i.e. the modes $m \neq 0$ are identical to those in (2.16) whereas the $m = 0$ mode is the sum of the base flow and the axisymmetric nonlinear perturbation:

$$\boldsymbol{v}_m \equiv \boldsymbol{v}'_m, \quad p_m \equiv p'_m, \quad m \neq 0, \tag{3.2a}$$

$$\boldsymbol{v}_0 \equiv \boldsymbol{V} + \boldsymbol{v}'_0, \quad p_0 \equiv P + p'_0. \tag{3.2b}$$

A system of coupled partial differential equations depending on the variables r and z (given explicitly in the Appendix § A.1) is resolved. For its time integration a classical time splitting method (Ronquist 1988) is used. The spatial discretization is based on the spectral-element decomposition (Patera 1984).

Although it has been shown that with an appropriate choice of the origin of the azimuthal coordinate, the computed modes will be real, the numerical implementation allows for complex modes. This makes it possible to simulate swirling flows. In the

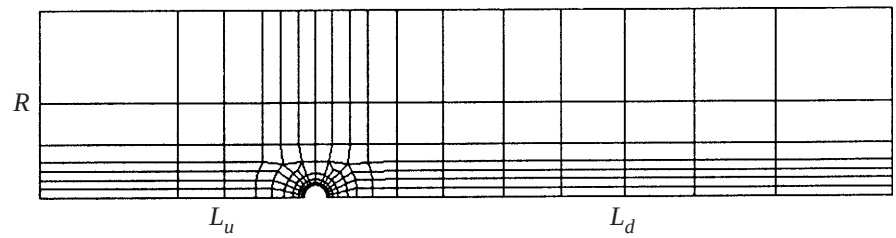

FIGURE 3. Spectral element discretization of the computational domain: R is the domain radius, L_u the upstream extent, L_d the downstream extent. The 'basic domain' corresponds to the subdomain with all the outer elements dropped.

present case, it provides a numerical means of testing the theoretical conclusion concerning the arbitrariness of the symmetry-plane orientation and its conservation once it is selected.

The axisymmetry-breaking instability was first generated by numerical noise. As a result, the selected symmetry plane did not coincide with the $\theta = 0$ plane and all resulting azimuthal modes had non-zero both real and imaginary parts. The rotation angle β from (2.15) was computed at one point of the flow for the axial velocity of the $m = 1$ mode. This value was then used to rotate the whole flow field around the flow axis. The plane symmetry is proved by the fact that the modes so obtained (2.16) are real, i.e. that their imaginary parts are identically zero everywhere in the flow. The numerical verification of the stability of the plane is given by the observation that these imaginary parts then remain exactly zero without any control of the symmetry-plane direction.

4. Computational domain, mesh optimization and primary instability threshold

The physical domain is cylindrical with the sphere placed on its axis. It can be generated by a rotation of the (z, r)-domain represented in figure 3. The (z, r)-domain is broken up into spectral elements as indicated in the figure. In the tests presented below, each spectral element contained 6×6 to 10×10 collocation points. The axis of the cylindrical domain is parallel to the flow direction. The sphere is placed on the axis of the domain at a distance L_u from the domain inflow and L_d from the domain outflow. The overall length of the domain is the sum of its upstream length and downstream length $L_u + L_d$. The radius of the domain is denoted R. The boundary conditions simulate an inflow at the upstream cylinder basis and an outflow elsewhere. The inflow boundary condition is a uniform velocity profile $u = U_\infty$, $v = w = 0$, the outflow condition consists in setting a zero pressure and zero viscous stresses in a weak sense. In Dušek *et al.* (1994*b*) and Dušek (1996) it has been shown that these weak Neumann outflow boundary conditions appear to be non-reflective, let the vortical structures leave the computational domain freely, deform very little the outflowing vortex structures (the deformations are restricted to the last element) and, most importantly, allow the computational domain to be truncated relatively close to the obstacle without a significant impact on the instability characteristics. For simulating a jet flow Dănăilă *et al.* (1997) find that it is efficient to use the same outflow condition on the lateral cylinder wall. For the jet this condition allows the aspiration of the surrounding fluid by the jet; for the present case it limits the blockage effect of Dirichlet boundary conditions.

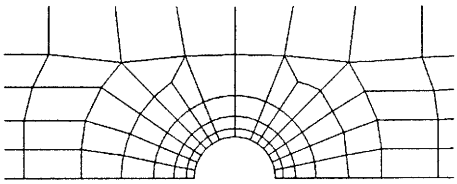

FIGURE 4. Detail of the mesh near the sphere.

The spectral-element mesh discretizing the (z,r)-plane has been optimized with respect to the following parameters:

(i) upstream domain extent,
(ii) downstream domain extent,
(iii) domain radius,
(iv) domain breakup into spectral elements,
(v) degree of interpolation polynomials (number of collocation points per spatial direction) of spectral elements.

A partial test consisted in comparing the recirculation length and the detachment angle to the data given by Fornberg (1988) and Johnson & Patel (1999) at $Re = 200$ (see the Appendix § A.2).

As the result of the tests described in the Appendix § A.2. we retain the following mesh throughout the remainder of the paper (except § A.3 where the possibility of reduction of computing costs is discussed):

$$L_u = 12d, \quad L_d = 25d, \quad R = 8d, \quad N_{order} = 6.$$

With this mesh the primary instability threshold is $Re_1 = 210.8$. An inspection of the test results shows that this value slightly underpredicts the exact threshold. A simple analysis of the data of the Appendix § A.2 gives a quantitative estimate of the underprediction and shows that the threshold lies slightly above $Re_1 \approx 212$ which is in excellent agreement with the value of Tomboulides *et al.* (1993).

The last parameter to optimize is the number of azimuthal Fourier modes to take into account in (2.5). The higher-order azimuthal modes are generated by nonlinear couplings and, as explained in § 2, to reach a given accuracy, the required number of azimuthal modes increases with increasing Reynolds number. A good measure of the effect of truncating the azimuthal Fourier expansion is the saturation amplitude of the fundamental azimuthal Fourier mode. Results of the tests carried out at $Re = 250$ are given in the next section. At the secondary (Hopf-type) bifurcation, similar tests carried out in § 6 check the dependence of the amplification rate of the secondary instability.

5. Steady non-axisymmetric flow

The steady non-axisymmetric flow has been investigated more closely for two Reynolds number values: $Re = 215$ and $Re = 250$. The first one has been chosen as a compromise between the proximity to the threshold and the computing costs necessary to obtain a satisfactory relaxation of the transients and to converge to the stable solution. As can be seen by evaluating the linear stability of the fixed point $|A| = \sqrt{\lambda/C}$ of (2.28), the solution converges theoretically to the fixed point as $\mathrm{e}^{-2\lambda t}$, λ being the unstable eigenvalue, i.e. the amplification rate of the instability. Close to the instability threshold the convergence is thus rather slow. Indeed, the $m = 1$ mode was found to converge exponentially to its asymptotic value with a convergence

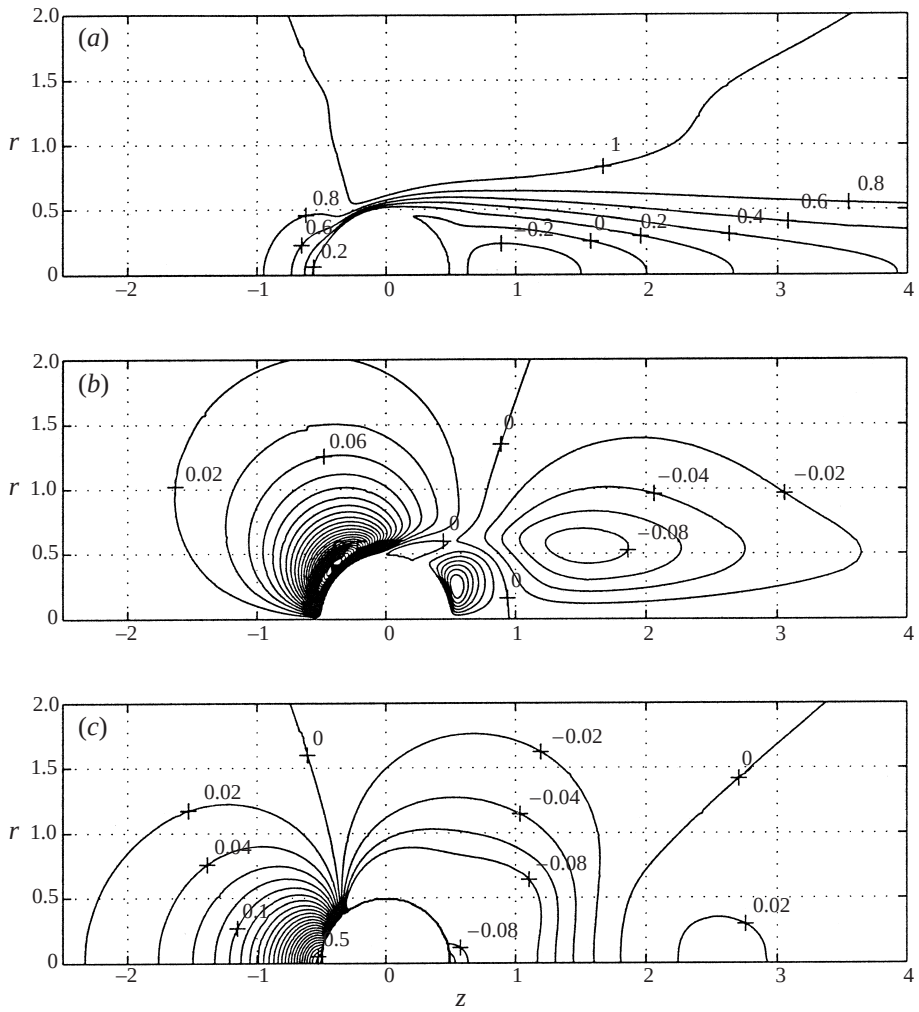

FIGURE 5. (*a*) Axial velocity, (*b*) radial velocity and (*c*) pressure of the base flow at $Re = 215$.

rate of $\lambda = -0.0168$, the amplification rate of the instability being $\lambda = 0.0119$. The slower convergence rate than expected can be attributed to higher-order effects. Our simulation approached the asymptotic value within 0.13%. The second Reynolds number value has been chosen to provide an easy comparison with other work (Tomboulides *et al.* 1993, Johnson & Patel 1999).

5.1. *Base flow*

For Hopf bifurcations it appears to be of great interest to investigate the difference between the unstable steady flow and the time mean value of the unsteady flow. Indeed, in Carte *et al.* (1996), Dušek (1996) and Zielinska *et al.* (1997) it was shown that there is sometimes a significant difference between the base flow and the mean value. In the present case of a symmetry-breaking instability, the analogous issue concerns the base flow $\boldsymbol{V}$ and the axisymmetric mode $\boldsymbol{v}_0$ of the azimuthal Fourier expansion (3.1), which are different entities. The base flow is computed by solving

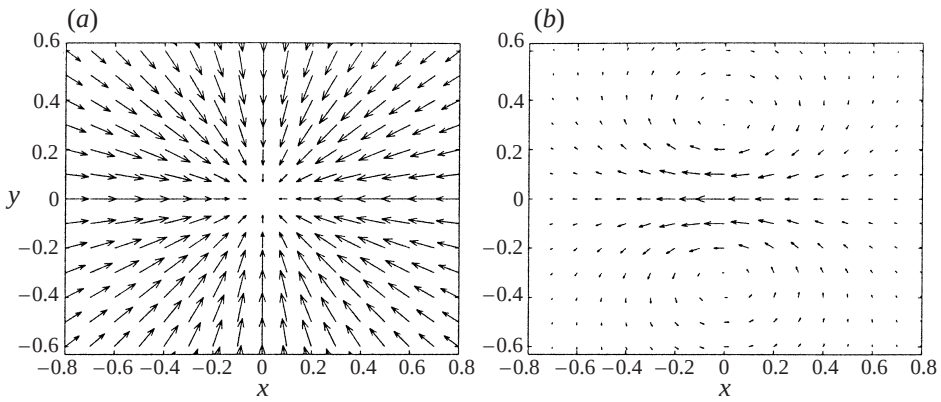

FIGURE 6. Transverse velocity field of the base flow (*a*) and of the $m = 1$ azimuthal mode (*b*) in the $z = 3$ plane for $Re = 215$.

the axisymmetric problem and provides the basis for computing the axisymmetric correction $\boldsymbol{v}'_0$ via the second equation (3.2).

In figure 5 we give the two velocity components and the pressure of the base flow (unperturbed axisymmetric flow) at $Re = 215$.

The representation of the axial velocity allows the recirculation zone to be located. At $Re = 215$, the recirculation length is $\ell_{b,215} = 2.0$, at $Re = 250$ it becomes (see figure 10) $\ell_{b,250} = 2.123$. In the case of the axisymmetric base flow the interpretation of the radial velocity plot is also straightforward, the zone of negative radial velocity meaning convergence of flow toward the flow axis, that of positive radial velocity in the recirculation zone corresponding to the divergence outward from the flow axis, and both zones indicate the position of the ring vortex. It may, however, be more meaningful to present transverse cuts of the velocity field. The plot of the transverse velocity field in the $z = 3$ plane is given in figure 6.

5.2. *Linear mode*

In figure 7 we represent the linear unstable mode at $Re = 215$ with the normalization chosen so that the maximum of the radial velocity component $\varphi_{r,1}$ is equal to one. This maximum lies on the flow axis at $z = 1.57$ for this Reynolds number value.

The appearance of the mode is that given by Natarajan & Acrivos (1993). With account of (2.15), in which we take β equal to π, the effect of the axial velocity component of the unstable mode (negative in figure 7, but multiplied by $\cos\pi = -1$) can easily be interpreted as acceleration of the flow in the $\theta = 0$ half-plane and deceleration in the $\theta = \pi$ half-plane. This corresponds to the shift of the maximum velocity deficit to this half-plane.

The interpretation of the radial and azimuthal velocity components is easier if the transverse velocity is represented in Cartesian coordinates in a transverse section of the flow. The $z = 3$ plane has been chosen in figure 6 for this purpose. It is seen that the linear mode is characterized by two counter-rotating modal vortical structures, the vorticities of which compensate exactly in accordance with the vorticity conservation principle. In figure 6 and in what follows, the axes are chosen so that the radial velocity component of mode $m = 1$ is negative along the x-axis. As a result, if the base flow and $m = 1$ mode are superimposed, the convergence point of the transverse cross-section will be shifted towards the negative x-axis; moreover, the vortical structures might appear in the resulting flow if the $m = 1$ mode is sufficiently strong.

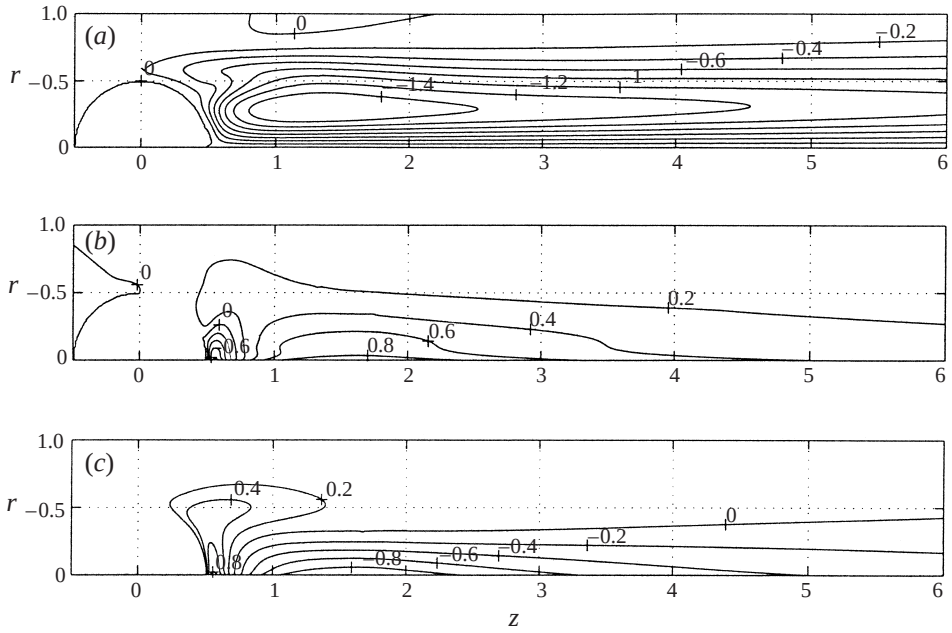

FIGURE 7. Normalized linear unstable mode at $Re = 215$. (*a*) The axial velocity, (*b*) the radial velocity, (*c*) the azimuthal velocity. The normalization is such that the maximum of the absolute value of the radial velocity is equal to one.

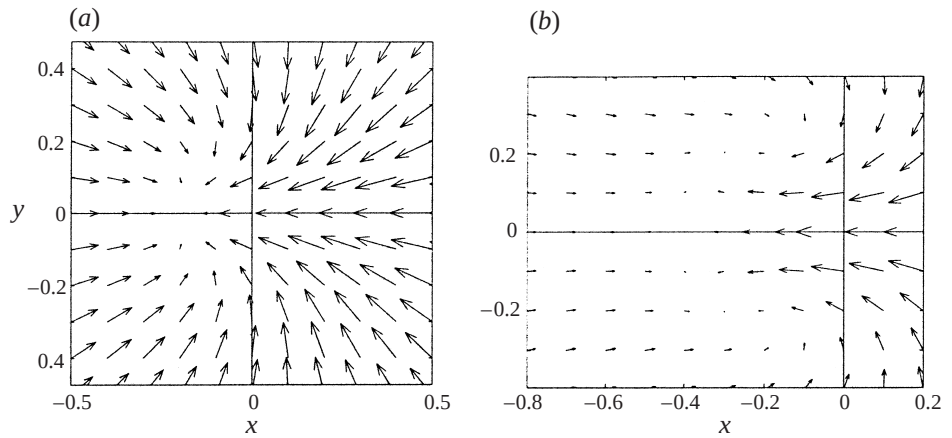

FIGURE 8. Transverse section of the flow field for a weak (*a*) and a strong (*b*) perturbation.

The velocity perturbation represented in figure 6(*b*) is combined with a varying amplitude depending on the instability development with the axisymmetric base flow of figure 6(*a*). The resulting flow is represented in figure 8 for a weak and a strong perturbation.

If a dye is injected into the flow, it is clear that in figure 8(*a*) it will concentrate at a single point corresponding to only one 'thread' present in the wake. In the case of a weak perturbation the vortices do not appear on the background of the axisymmetric flow and their net effect is reduced to shifting the thread off the flow axis. The onset

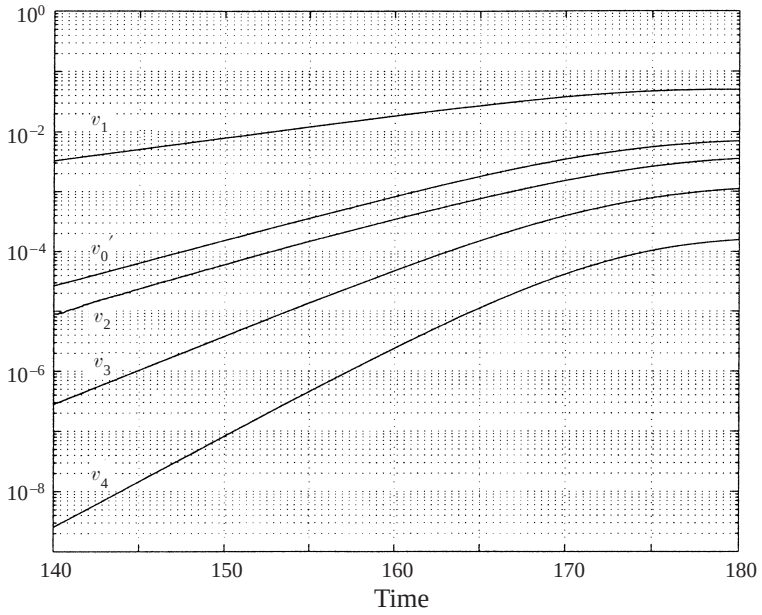

FIGURE 9. Linear amplification and saturation of the radial component of $m = 1$ to $m = 4$ azimuthal modes $v_1 \ldots v_4$ and of the axisymmetric correction v_0' at $Re = 250$ at the point $z = 1.536\,d$, $r = 0.107\,d$. Note the identical slope of v_0' and of v_2.

	v_0'	v_1	v_2	v_3	v_4
$Re = 215$	–	0.00797	0.0159	0.0243	–
$Re = 250$	0.178	0.0856	0.170	0.256	0.341

TABLE 2. Amplification rates of the first four azimuthal harmonics and of the axisymmetric correction in the linear regime of instability amplification at the same point as in figure 9. At $Re = 250$ the amplification rates correspond to the slopes of the straight parts of the curves represented in figure 9. At $Re = 215$ the axisymmetric correction and the $m = 4$ mode were too weak.

of a 'bifid' wake is illustrated by figure 8(*b*) where the two counter-rotating vortices of the linear perturbation are strong enough to appear in spite of the presence of the base flow.

The radial velocity of the base flow and the linear mode vary in the streamwise direction so that the resulting effect is not necessarily the same everywhere. There may be a zone where the wake has only one thread to split, farther downstream, into a bifid wake. A more detailed discussion of this will be given in § 5.7.

5.3. *Instability saturation*

If nonlinear couplings between the individual modes are switched on the exponential growth observed for the linear mode saturates when a sufficient amplitude is reached.

In figure 9 we compare the amplification of the fundamental $m = 1$ mode v_1 to that of the axisymmetric correction v_0' and of modes v_2, v_3, v_4 at the same point $z = 1.536\,d$, $r = 0.1074\,d$ at $Re = 250$. The graph presents the growth from a level corresponding to about 1% of the saturation and captures the linear regime (stage of

	$m_{max}=1$	$m_{max}=2$	$m_{max}=3$	$m_{max}=4$
$\max(\|v_1\|)$	6.446×10^{-2}	6.439×10^{-2}	6.464×10^{-2}	6.452×10^{-2}
z_{max}	1.66	1.62	1.62	1.62

TABLE 3. Variation of the maximum value of the radial component of the $m=1$ azimuthal mode and of its axial position z_{max} ($r_{max}=0$) at saturation for $Re=250$ for a varying number m_{max} of azimuthal modes taken into account.

exponential amplification) and the saturation of all Fourier modes of the instability settling to the fixed point. The amplification rates in the linear regime are given also for both $Re=215$ and $Re=250$ in table 2.

In accordance with the theory of § 2 the amplification rate of the m-mode is equal to m times that of the fundamental mode. That of the axisymmetric correction is equal to twice the amplification rate of the fundamental mode (see (2.26), (2.27), respectively).

Higher-order modes are theoretically increasingly important above the instability threshold. The number of relevant modes is tested in table 3 where we present the dependence of the maximum of the v_1 component at saturation on the number of azimuthal modes taken into account. We conclude that even at $Re=250$ three modes $(0,1,2)$ account very well for the saturation of the instability. Adding the third and the fourth mode yields only a 0.29% variation of the saturation value at $Re=250$. The inaccuracies due to an insufficient number of azimuthal modes can very easily be made negligible. The only inaccuracy that remains is that of the spectral-element meshing resulting in about a 1% underprediction of instability threshold.

The most important coupling appears to be that between the $m=1$ and $m=0$ modes. The influence of other modes on the saturation level is relatively weak, especially close to the instability threshold. We encounter the same surprising effect as for the Hopf bifurcation in the cylinder wake (Carte *et al.* 1996). In contrast with theoretical expectations according to which the nonlinear correction of the axisymmetric flow and the $m=0$ mode are of the same order, the effect of the $m=2$ mode on the saturation is much weaker, which is easily explicable by the fact that the axisymmetric correction (figure 10) is about 7 times stronger than the $m=2$ mode (figure 12).

5.4. *Non-linear axisymmetric correction*

As we have just seen, the coupling between the fundamental and the $m=0$ mode is basically responsible for the instability saturation. This coupling generates a nonlinear axisymmetric correction to the base flow. The latter is obtained as the difference between the axisymmetric mode obtained at saturation and that of the base flow. Figure 10 presents the axial component of the base flow velocity, its nonlinear correction and the resulting $m=0$ mode at $Re=250$.

The figure shows that the nonlinear axisymmetric correction tends to reduce the velocity deficit everywhere. This results in a shallower and shorter recirculation zone of the $m=0$ mode compared to the base flow. In Zielinska *et al.* (1997) it has been pointed out that the onset of the Hopf-type instability in the cylinder wake reverses the trend of growth of the recirculation zone: while in the subcritical and steady base flow the recirculation length grows with increasing Reynolds number, the time

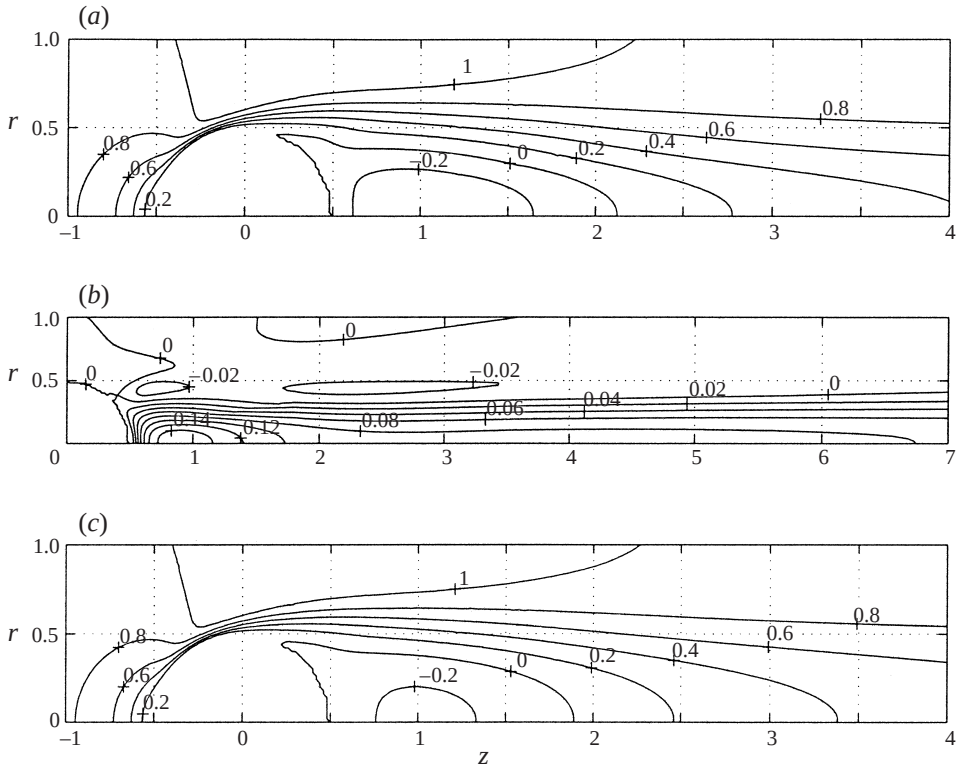

FIGURE 10. Axial velocity component of the base flow at $Re = 250$ (*a*), axisymmetric nonlinear correction (*b*) and the full nonlinear $m = 0$ mode (*c*).

	$Re = 215$	$Re = 250$
Base flow	2.00	2.123
$m = 0$	1.9654	1.8901

TABLE 4. Increase of the recirculation length for the base flow and decrease for the nonlinear axisymmetric ($m = 0$) mode when Re varies from 215 to 250.

average of the unsteady supercritical flow has a decreasing recirculation length. Here we observe the same effect of the symmetry-breaking instability (see table 4).

5.5. *Saturated $m = 1$ mode*

It is known that the saturated fundamental mode of a Hopf bifurcation is deformed in comparison with the linear mode (see Carte *et al.* 1996). We find the same behaviour for the regular instability investigated in this paper. The axial velocity component u_1 of the mode $m = 1$ is compared to the same component of the linear mode in figure 11 obtained at $Re = 250$. It is interesting to note that, unlike for the unsteady infinite cylinder wake of Dušek (1996) or the after-body wake of Carte *et al.* (1996), the nonlinear effects contribute to an extension rather than a shrinking of the mode. The nonlinear mode has a maximum lying farther downstream than that of the linear mode (at $z = 1.3$) and the mode decays more slowly downstream.

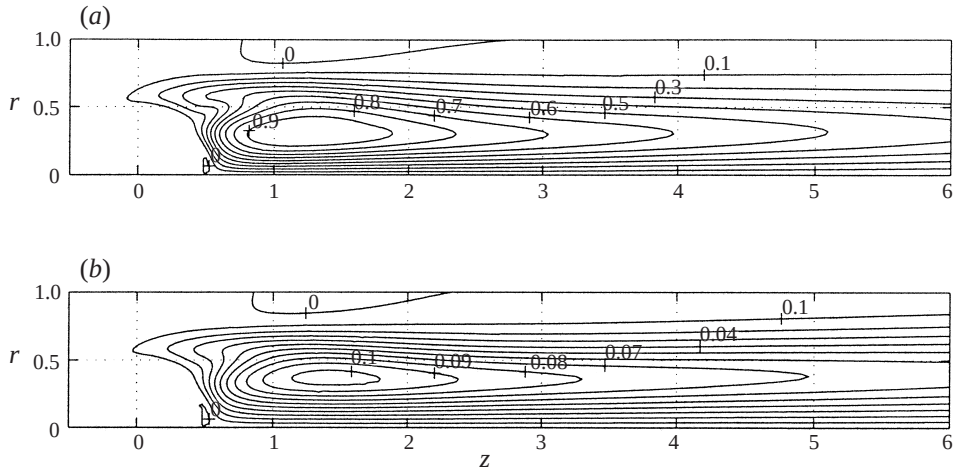

FIGURE 11. (*a*) Axial velocity component of the linear mode normalized so that its maximum (at $z = 1.14$ and $r = 0.3$) is equal to 1. (*b*) $m = 1$ mode.

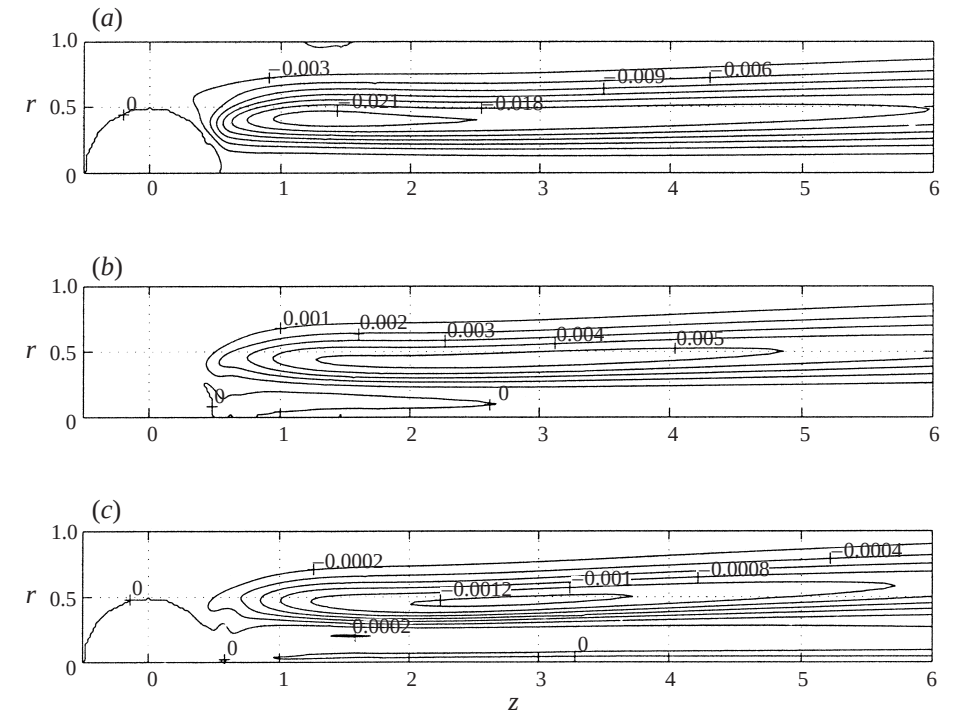

FIGURE 12. Axial component of the $m = 2$, $m = 3$ and $m = 4$ azimuthal mode at $Re = 250$.

5.6. *Higher-order modes*

Considered in the (z, r)-plane and in cylindrical coordinates the higher-order modes present a similar structure to the fundamental mode with the only difference that all velocity components are zero at the flow axis for $m > 1$. In figure 12 we give the axial component of the $m = 2$, $m = 3$ and $m = 4$ azimuthal mode at $Re = 250$. The maxima of the absolute values of the modes decrease, on average, by a

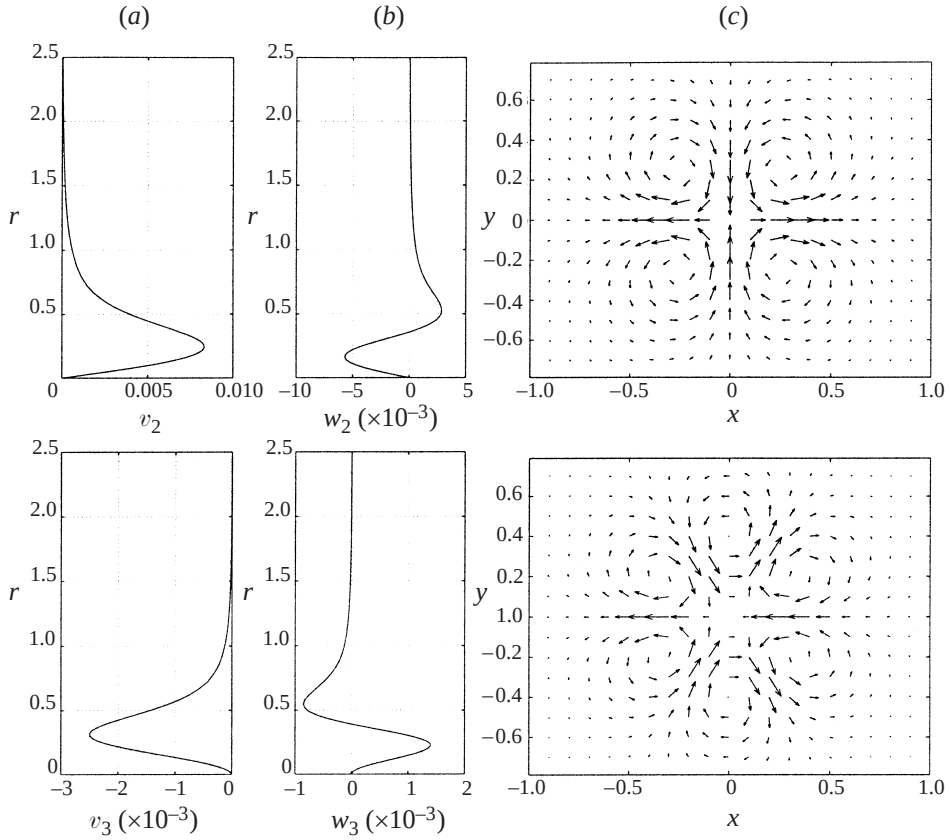

FIGURE 13. Radial profiles of (*a*) the radial and (*b*) azimuthal components, and (*c*) the cross-section represented in Cartesian coordinates for the $m = 2$ mode (top) and $m = 3$ mode (bottom). The profiles and cross-sections are represented in the plane $z = 3$.

factor $|u_m|_{max}/|u_{m+1}|_{max} = 4.4$. The radial component has a similar appearance with a maximum in each z-plane lying slightly closer to the flow axis (at $r \approx 0.3$). The azimuthal component changes sign to form vortices that can be described in a more conventional way in Cartesian coordinates.

Indeed, if represented in Cartesian coordinates, the transverse velocity of the mth mode taken in a transverse plane presents m pairs of counter-rotating vortical structures as seen in figure 13, which shows the radial profiles of the radial and azimuthal components of the $m = 2$ and $m = 3$ modes and the resulting flow cross-sections.

5.7. *Bifid wake*

As stated in the introduction, the existence of one or two threads in the wake visualized by dye injection has been the subject of controversy in many previous papers. In § 5.2 we have explained that the presence of a single or of a double wake depends on the magnitude of the symmetry-breaking perturbation. The fundamental $m = 1$ mode is the most important; the higher-order modes are practically irrelevant as has been shown by modelling the onset of the bifid wake by a simple superposition of the base flow and of the linear mode taken with two different amplitudes. The picture provided by a cross-section in a given z-plane is, however, incomplete. Although the difference

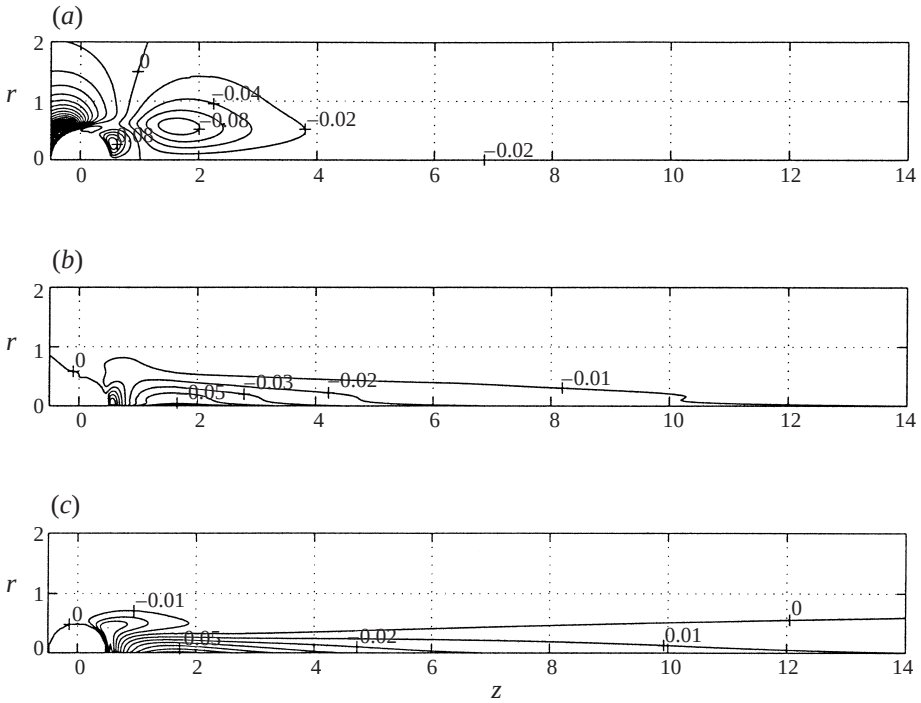

FIGURE 14. Radial velocity component of the $m = 0$ mode (a), and radial (b) and azimuthal (c) velocity components of the $m = 1$ mode at $Re = 250$.

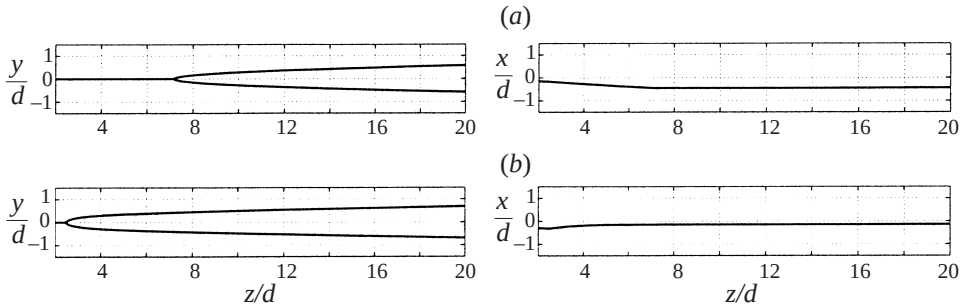

FIGURE 15. Loci of convergence points of the transverse flow field coinciding with experimental dye threads. (a) $Re = 215$, (b) $Re = 250$, left: projection normal to the symmetry plane, right: projection onto the symmetry plane.

between the base flow and the linear mode on one side and the $m = 0$ and $m = 1$ mode including nonlinear effects on the other side is qualitatively insignificant we shall analyse the onset of the bifid wake in a completely realistic way by investigating the superposition of the $m = 0$ and $m = 1$ modes at $Re = 215$ and $Re = 250$ in the whole domain downstream of the sphere. As can be seen in figures 5 and 7 the radial component of the axisymmetric flow decays more rapidly than the radial and azimuthal components of the linear mode. This is also the case for the $m = 0$ and $m = 1$ modes represented at $Re = 250$ in figure 14.

If the modes $m = 0$ and $m = 1$ are combined in the same way as described in § 5.2 it is possible to locate the points of convergence characterized by a zero transverse

velocity in each z-plane. The locus of such points represents the threads in which a dye would concentrate downstream of the recirculation zone. The result is given in figure 15 at $Re = 215$ and $Re = 250$. It can be seen that for both Reynolds numbers the picture is qualitatively similar. The threads form a pitchfork-like pattern, the branch point lying farther downstream for the lower Reynolds number value. It can be concluded that there always exists a zone of the wake close to the sphere where only one thread exists and there always exists a double thread wake sufficiently far downstream. The double thread necessarily exists sufficiently far downstream due to the rapid decay of the radial $m = 0$ mode component but it may not be experimentally observable if the branch point is situated too far downstream. On the other hand, at $Re = 250$ the branch point is situated inside the recirculation zone which would be filled entirely with dye in an experimental visualization and only two threads would be visible.

It is interesting to note that the flow visualization does not necessarily reveal vortical structures so that it is not surprising that spatial representation of the vorticity distribution such as that used in Johnson & Patel (1999) based on the method of Jeong & Hussain (1995) yields a different picture than dye advection in experiments (see Ormières 1999; Provansal & Ormières 1997*b*).

6. Onset of unsteadiness

6.1. *Plane-symmetry conservation at the secondary instability*

In §§ 2, 3, it has been shown that the most appropriate description of the steady non-axisymmetric state of the wake is the azimuthal Fourier expansion (3.1). The flow is thus described by the infinite array of azimuthal modes $\boldsymbol{v}_m, p_m$ investigated in the previous section. The fact that axisymmetry breaking leads to plane symmetry with respect to a plane containing the flow axis selected arbitrarily by the initial conditions or by any small symmetry perturbation has been interpreted mathematically in terms of the existence of a real solution of the system of coupled equations (2.17). This real solution corresponds to the azimuthal mode expansion with the origin of the azimuthal angle θ taken in the symmetry plane. As a result, the non-axisymmetric state of the wake is described fully by an array of azimuthal velocity modes – real vectorial functions of two variables z and r:

$$\mathscr{V} \equiv \{\boldsymbol{v}_m\}_{m=0}^{\infty}. \tag{6.1}$$

(Modes with negative indices coincide with those with positive ones: $\boldsymbol{v}_{-m} = \boldsymbol{v}_m$. The pressure modes can be considered as auxiliary variables.) As a result, the system (2.17) can be written in an abridged form as

$$\frac{\partial \mathscr{V}}{\partial t} = \mathscr{N}[\mathscr{V}], \tag{6.2}$$

$\mathscr{N}$ symbolizing the nonlinear operator acting on the array of velocity modes defined in (2.17). In § 2 this operator has been shown to be real, i.e. to transform a real array into a real one. We have thus the case of a real dynamical system such as that of a flow field undergoing a primary Hopf instability with the only difference that the state of the flow is no longer characterized by just one real vector field but by a whole array. The non-axisymmetric steady solution represents a fixed point for which $\mathscr{N}[\mathscr{V}_o] = 0$. At the secondary instability this fixed point undergoes a Hopf bifurcation with a pair of complex-conjugate eigenvalues crossing the imaginary axis, becomes unstable but remains real. The effect of the Hopf bifurcation consists just in replacing the steady array of real vector fields by an unsteady array $\mathscr{V}(t)$. The azimuthal

expansion coefficients remaining real, the plane symmetry $u(z,r,\theta,t) = u(z,r,-\theta,t)$, $v(z,r,\theta,t) = v(z,r,-\theta,t)$, $w(z,r,\theta,t) = -w(z,r,-\theta,t)$ is conserved if the flow field is re-composed via the azimuthal expansion (3.1).

The new unsteady solution will settle to a limit cycle, i.e. it will become periodic with the same period T throughout the flow field. A thorough verification of this property has been given in Dušek *et al.* (1994*b*) for a two-dimensional cylinder wake and the same holds for the present case. The array $\mathscr{V}(t)$ can thus be expanded into a time Fourier series, the fundamental mode of which is closely linked to the linear unstable mode and the higher-order harmonics of which correspond to higher-order nonlinear modes of the Hopf-type instability. Expanding the array $\mathscr{V}(t)$ amounts to expanding each of its components into a series:

$$\boldsymbol{v}_m(z,r,t) = \sum_{n=-\infty}^{\infty} \boldsymbol{c}_{n,m}(z,r)\, \mathrm{e}^{\mathrm{i}n\omega t}, \tag{6.3}$$

where $\omega = 2\pi/T$ is the angular frequency of oscillations at the limit cycle. The pressure modes will be expanded into

$$p_m(z,r,t) = \sum_{n=-\infty}^{\infty} d_{n,m}(z,r)\, \mathrm{e}^{\mathrm{i}n\omega t}. \tag{6.4}$$

Expansions (6.3) and (6.4) can be substituted into (3.1) to reconstitute the unsteady non-axisymmetric velocity and pressure fields. To yield real sums the complex Fourier modes satisfy $\boldsymbol{c}_{-n,m}(z,r) = \overline{\boldsymbol{c}_{n,m}(z,r)}$ and $d_{-n,m}(z,r) = \overline{d_{n,m}(z,r)}$. Plots and analysis of some time Fourier modes will be given in § 6.3.

6.2. *Instability onset and development*

The formalism of the previous subsection makes it obvious that the unsteady perturbation $\mathscr{V}'$ of the fixed point $\mathscr{V}_0$ amplified in the linear regime will be described as

$$\mathscr{V}' = \alpha\, \boldsymbol{\Psi}\, \mathrm{e}^{(\gamma+\mathrm{i}\omega_0)t} + \text{c.c.}, \tag{6.5}$$

with $\gamma + \mathrm{i}\omega_0$ and $\boldsymbol{\Psi}$ representing, respectively, the unstable eigenvalue and the associated eigensolution of the linearized problem (6.2). The linear eigenmode is an array of complex vector fields in the (z,r)-plane. As a result, the instability onset, its amplification rate γ and angular frequency ω_0 can be monitored for any azimuthal mode, any velocity component (or pressure) and anywhere in the (z,r)-plane.

The threshold of the secondary instability has been determined by investigating the dependence of the amplification rate of the instability on the Reynolds number. For this purpose, close to the expected threshold, a solution presenting oscillations of very small amplitude was computed at $Re = 270$ and $Re = 275$ in the linear regime (with exponential decay or amplification of oscillations) considering azimuthal modes $m = 0$ to $m = 4$. The amplification rates were determined by analysing the oscillation amplitude of the radial component of the $m = 1$ azimuthal mode at the point $z = 0.78$ and $r = 0$, chosen because this mode is non-zero along the flow axis and because close to the sphere the initial value transients are expelled earlier than in the far wake. The amplification rates found, -7.07×10^{-3} and 7.87×10^{-3}, respectively, allow the instability threshold to be situated at $Re_2 = 272.3$. A very interesting issue is the question of how many azimuthal modes are necessary to capture the secondary instability. The tests of the influence of the size of the azimuthal mode basis on the instability threshold showed that, even if only $m = 0$ and $m = 1$ modes are considered,

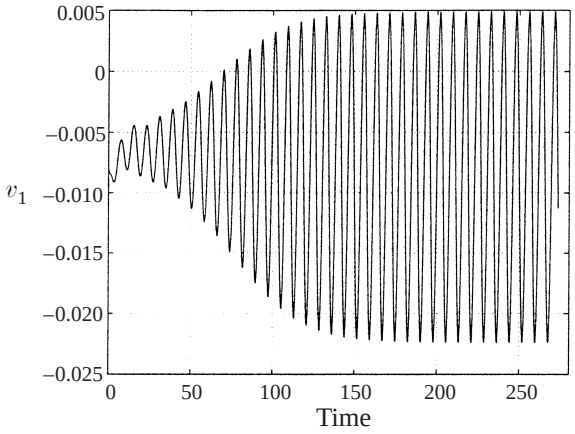

FIGURE 16. Amplification of small oscillations and saturation at $Re = 280$. The figure represents the local signal at $r = 0$ and $z = 0.78$ of the radial component of the $m = 1$ azimuthal mode.

	γ	C_r	ω_0	C_i	C_i/C_r
Linear regression	0.02676	−144.77	0.8011	65.88	−0.4551
Quadratic regression	0.02973	−207.82	0.7996	98.49	−0.4739

TABLE 5. Landau model coefficients $(1/A)\,\mathrm{d}A/\mathrm{d}t = \gamma - C_r A^2$, $\omega = \omega_0 - C_i A^2$ obtained by a linear and quadratic regression of the graphs in figure 17. Note that the globally relevant coefficients (γ, ω_0 and C_i/C_r) are fairly independent of the degree of regression.

the instability sets in, although at a higher Reynolds number ($Re \approx 286$). Adding further modes improves the quantitative accuracy very rapidly. The extension of the basis to $m = 5$ and $m = 6$ modes increases the value of the amplification rate of the secondary instability at $Re = 275$ from 7.87×10^{-3} to 7.91×10^{-3}, i.e. yields a negative correction to the critical Reynolds number of less than 0.03. The value of $Re_2 = 272.3$ found is thus subjected only to errors of the spectral-element meshing on the (z, r)-plane. Taking account of the error estimates of § 5 and of the fact that the mesh inaccuracy results systematically in an underprediction of the instability threshold, the exact value is situated very likely between $Re = 272.3$ and $Re = 275$, which is in a good agreement with the experimental value of Provansal & Ormières (1997*a*) ($Re_2 = 273$). The critical Strouhal number was found to be $St_{crit} = 0.127$.

At $Re = 280$ the transients are long enough for a satisfactorily accurate analysis and short enough to be simulated at acceptable cost. The signal obtained for the same mode, velocity component and point as above is presented in figure 16. It is interesting to see to what extent a third-order nonlinear theory and the Landau model applies to the computed behaviour. For this purpose we have analysed the amplitude and frequency of oscillations in figure 16. The analysis consists simply in estimating the variable zero mode of the instability as the mean between subsequent minima and maxima and in taking the amplitudes and instantaneous periods with respect to this mean value. Both the logarithmic derivative $(1/A)\,\mathrm{d}A/\mathrm{d}t$ of the amplitude and the instantaneous angular frequency ω prove to be linear functions of the square of the amplitude A^2 with a fairly good accuracy (see figure 17). The Landau model coefficients obtained by linear regression are given in table 5. The nonlinear frequency

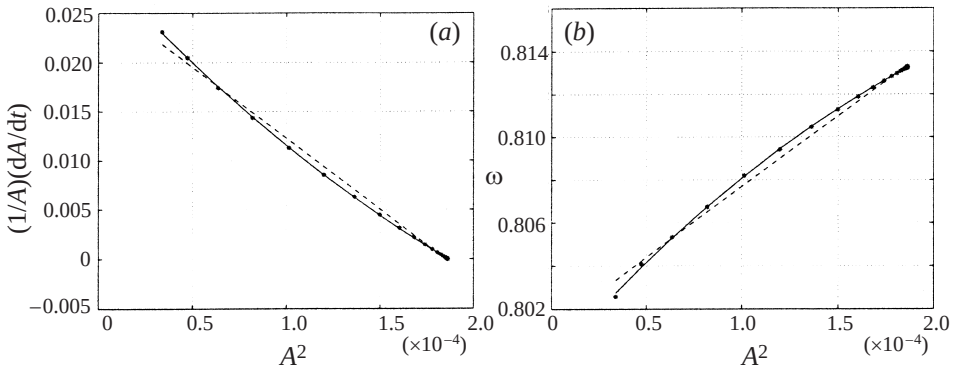

FIGURE 17. Logarithmic derivative of the oscillation amplitude (*a*) and instantaneous angular velocity (*b*) of the signal of figure 16. Dots (·) represent the calculated values for $(1/A)\,\mathrm{d}A/\mathrm{d}t$ (*a*) and ω (*b*), the dashed line is the linear fit and the full line is the quadratic fit.

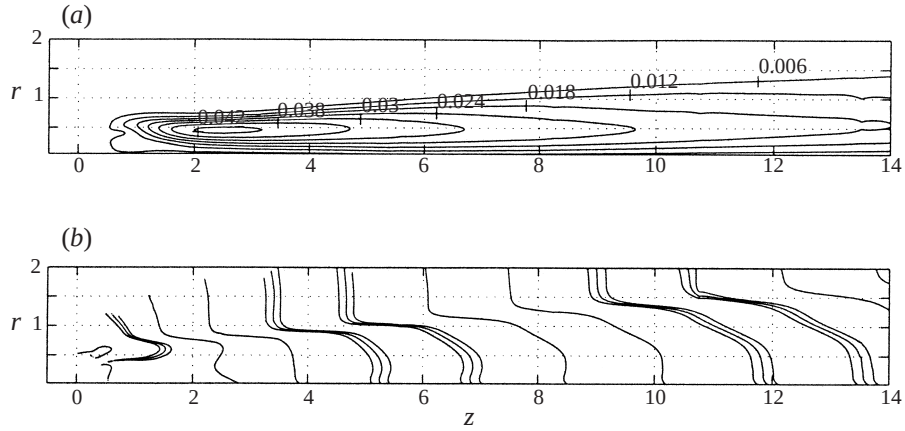

FIGURE 18. The time Fourier fundamental ($n = 1$) mode of the $m = 1$ azimuthal mode of the axial velocity ($c_{1,1;z,r}$ mode) at $Re = 300$. (*a*) Modulus (envelope of oscillations), (*b*) isolines of the cosine of the phase ϕ. The triple line corresponds to $\varphi = \pm\pi/4$, the simple line to $\phi = \pm\frac{3}{4}\pi$.

variation is very small. The angular frequency varies from 0.802 to 0.813 (in terms of Strouhal numbers from 0.1276 to 0.1294) i.e. by less than 2% in figure 17. The ratio C_i/C_r is of special interest because it represents an important global characteristics of the instability related to the difference $\Delta\omega = \omega_\infty - \omega_0$ between the angular velocity ω_∞ of oscillations at the limit cycle and the angular velocity ω_0 in the linear regime: $C_i/C_r = -\Delta\omega/\gamma$. Our simulation yields $C_i/C_r \approx -0.5$, the value obtained by linear and quadratic regression differing only by 4%. This is significantly less than for an infinite cylinder for which $C_i/C_r \approx -3$ (Sreenivasan, Strykowski & Olinger 1987; Dušek *et al.* 1994*b*).

6.3. *Limit cycle*

In § 6.1 we claim that an appropriate characterization of the limit cycle consists in investigating the coefficients of the double Fourier expansion of the flow (6.3), (6.4). The time Fourier modes indices will be denoted *n*, the azimuthal modes will again have the index *m*.

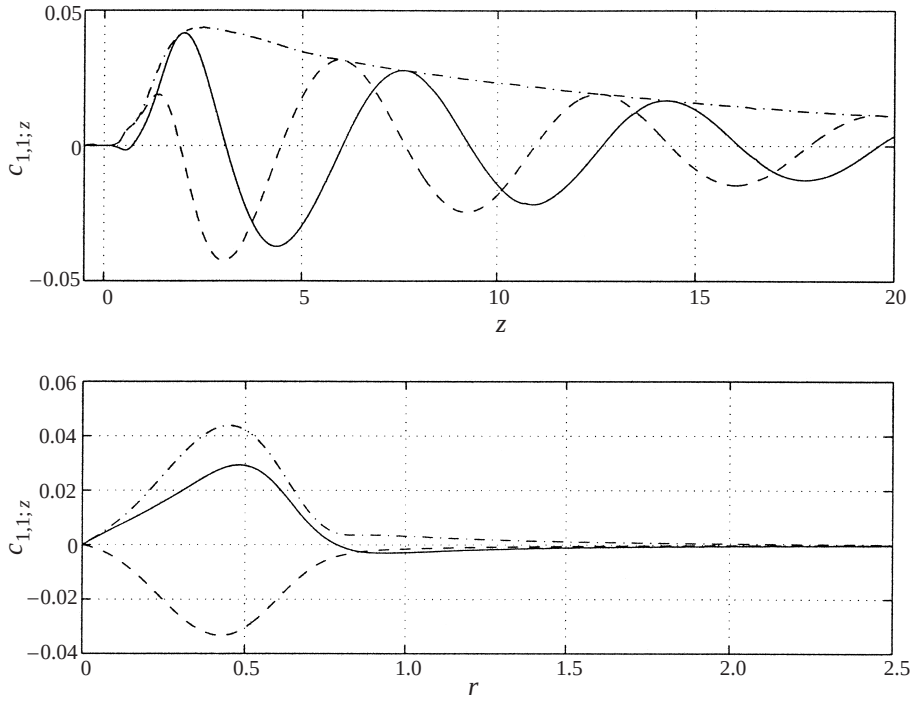

FIGURE 19. (*a*) Longitudinal and (*b*) transverse profiles for the axial velocity component of the mode $n = 1$, $m = 1$ at, respectively, $r = 0.46$ and $z = 2.5$. The full line and dashed line represent the real and imaginary parts of the mode and provide an image of instantaneous mode profiles at two instants differing by a quarter of a period. The dash-dotted line is the mode modulus.

As shown in the previous section, an azimuthal expansion truncated at $m = 4$ is largely sufficient to capture the secondary instability onset with accuracy. The next question is how the number of azimuthal modes influences the limit cycle. The effect of adding the 5th and 6th azimuthal mode to the $m = 0$ to $m = 4$ modes results in a 4% and 2% correction to the $m = 1$ mode oscillation amplitude at the point specified in the caption of figure 16. This might seem non-negligible; however, a local variation does not account for the global accuracy. A more global criterion consists in considering the variation of the maximum of the fundamental time Fourier mode $m = 1$, $n = 1$ represented in figure 18. If the total number of azimuthal modes is increased from $m_{max} = 5$ to $m_{max} = 6$ the maximum increases only by about 0.2%. (Note that the complex Fourier expansion (6.3) implies that the maximum 0.0438 of the mode modulus in figures 18 and 19 means twice that, i.e. 0.0876, in terms of the oscillation amplitude of the local signal.) The variations of the frequencies for m_{max} varying from 4 to 6 does not exceed 0.5%. The value of the Strouhal number found $St \approx 0.135$ lies slightly below those reported by Tomboulides *et al.* (1993) and Johnson & Patel (1999) and agrees with the experimental Strouhal number of the vortex shedding behind a sphere attached from the rear to a pipette making an angle of 10° with the flow axis given by Ormières (1999).

A global representation of the periodic state of the wake is obtained by representing the time–azimuthal Fourier modes (6.3) as two-dimensional plots in the (z, r)-plane. An example of such a representation is given in figure 18. The time Fourier modes being complex it is possible to represent either their real and imaginary parts or

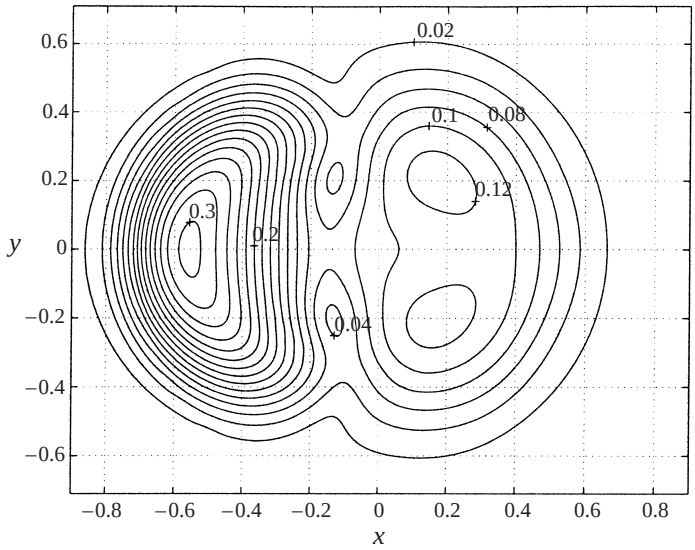

FIGURE 20. Cross-section of the flow representing the spatial distribution of the r.m.s. of fluctuations of the axial velocity in the $z = 3d$ plane. The maximum reached is 30.4% of inflow velocity.

their modulus and phase. The first alternative yields a more usual picture of the vortex street; however, the second one depicts much better the wave characteristics such as the envelope of oscillations, the wavelengths and transverse phase variations of the modes. The time Fourier modes are obtained by an on-line integration of the azimuthal modes at all discretization points during one oscillation period of the simulation. In Dušek (1996), it has been shown that the time Fourier modes provide much interesting information on the spatial structure of the wake of the infinite cylinder. The same holds for the sphere wake but a detailed description of even just the most significant modes falls outside the scope of this paper. Here we limit ourselves to pointing out some of the most important features allowing the interest of the time Fourier expansion to be assessed.

The unsteady wake behaves like a spatially modulated propagating wave. The maximum of the modulus of the streamwise component of the $n = 1$, $m = 1$ mode is reached at $z = 2.5$ and $r = 0.46$ and represents 4.4% of the inflow velocity (figure 18*a*). According to our notation of expansion coefficients (3.1) and (6.3), if only this mode were present in the flow, it would mean that the velocity fluctuations are 4 times 4.4% of the inflow velocity, i.e. 17.6%. This is because our expansions contain twice the same azimuthal mode and mutually complex-conjugate time modes. The experimental data of Ormières (1999) and the simulation of Johnson & Patel (1999) present the amplitude of oscillations in the form of r.m.s. fluctuations of the streamwise velocity component corresponding, mathematically, to

$$u_{r.m.s} = \left[2 \sum_{n=1}^{\infty} \left| c_{n,0;z} + 2 \sum_{m=1}^{\infty} c_{n,m,z} \cos m\theta \right|^2 \right]^{1/2}. \tag{6.6}$$

In figure 20, we represent $u_{r.m.s}$ for the flow cross-section at $z = 3$. The plot has been obtained by superposing $m = 0$ to $m = 6$ azimuthal modes and the $n = 1$ and $n = 2$ time modes. Interestingly, if only the $n = 1$ mode and $m = 0, 1, 2$ azimuthal

modes are taken into account the maximum (30.4% of the inflow velocity) decreases merely by about 3% and the plot is practically the same as in figure 20. The principal maximum and a secondary one appear in the symmetry plane and can be explained basically by the superposition of the $m = 1$ and $m = 0$ modes. The $m = 0$ mode being constant in the azimuthal direction whereas the $m = 1$ mode varies by 2π around the flow axis, the secondary maximum lies opposite the principal one. The two symmetrically placed secondary maxima are due to the $m = 2$ mode. The higher-order azimuthal modes contribute only quantitative corrections. The agreement with experimental fluctuation maps of Ormières (1999) is very good both qualitatively and quantitatively. At $Re = 300$ Ormières (1999) finds $u_{r.m.s.} = 27\%$ at the maximum situated close to $z = 3$ plane. Johnson & Patel (1999) do not provide a profile of the maxima of fluctuations. Their values are taken along the flow axis predicting $u_{r.m.s.} = 7.5\%$ at $z = 3$. Figure 20 yields about 9% at the flow axis.

The superposition of the $m = 0$ and $m = 1$ modes can also be analysed to provide an explanation for the onset of the hairpin vortices visible in flow visualizations and for the difference between the spatial picture of alternately shed vortical structures and the fact that the hairpins visible in flow visualizations are one sided and correspond only to every second vortical structure. The explanation comes basically from the cosine resulting from superposing the $m = \pm 1$ terms of the azimuthal expansion (3.1). Whereas for one direction, say $\theta = 0$, the $m = 1$ mode reverses locally the flow creating a vortex visualized by the advected dye, for $\theta = \pi$ the same term has an opposite sign and instead enhances the downstream advection and no dye concentration appears. A more detailed analysis of the link between flow visualizations and the limit cycle characteristics presented will be the topic of a separate article.

The propagating wave character of the flow oscillations is best illustrated by figure 18(*b*) where the cosine of the phase is plotted (see caption of the figure). It allows an estimate of the wavelength between $z = 7$ and $z = 14$ of about $7d$. This agrees very well with figure 33 of Johnson & Patel (1999). The phase picture shows other interesting features such as the phase advance of the outer region of the wake, which is easily explainable by a locally lower phase velocity in the near wake. The phase shift results in oscillations with opposite phases in zones delimited by the mixing layer of the wake which explains the change of sign of the instantaneous transverse profile of the mode in figure 19(*b*) and, eventually, it remains frozen in the far wake. In this way, the fingerprint of passing through the near-wake region remains conserved. The transverse phase variation is responsible for the formation of hairpin vortices.

Figures 18 and 19(*a*) show that the wavelength is a local feature depending on the downstream distance from the sphere and on the distance from the flow axis. In Ormières (1999) the wavelength is obtained by measuring the phase shift of oscillations along the flow axis. For the axial velocity component of the mode $m = 1$, $n = 1$ already presented the phase shift along a line parallel to, but $0.46d$ off, the flow axis is represented in figure 21(*a*). The z-derivative of the phase yields the streamwise wavenumber (figure 21*b*). It is immediately seen that the wavenumber (i.e. the wavelength) varies. It settles asymptotically to a value of $k_z \approx 0.9$ in the far wake. This value corresponds exactly to the wavelength of 7 sphere diameters estimated for figure 18 and in figure 33 of Johnson & Patel (1999). A similar analysis has to be done for all modes to obtain a good idea of the special signature of each mode. In this way it can be found that the $m = 0$, $n = 1$ mode of the axial velocity, dominant along the flow axis, has a wavenumber k_z exceeding the value of 1 between $z = 4$ and $z = 11$, reaching a local maximum $k_z = 1.1$ at $z = 9$. It is thus not contradictory to

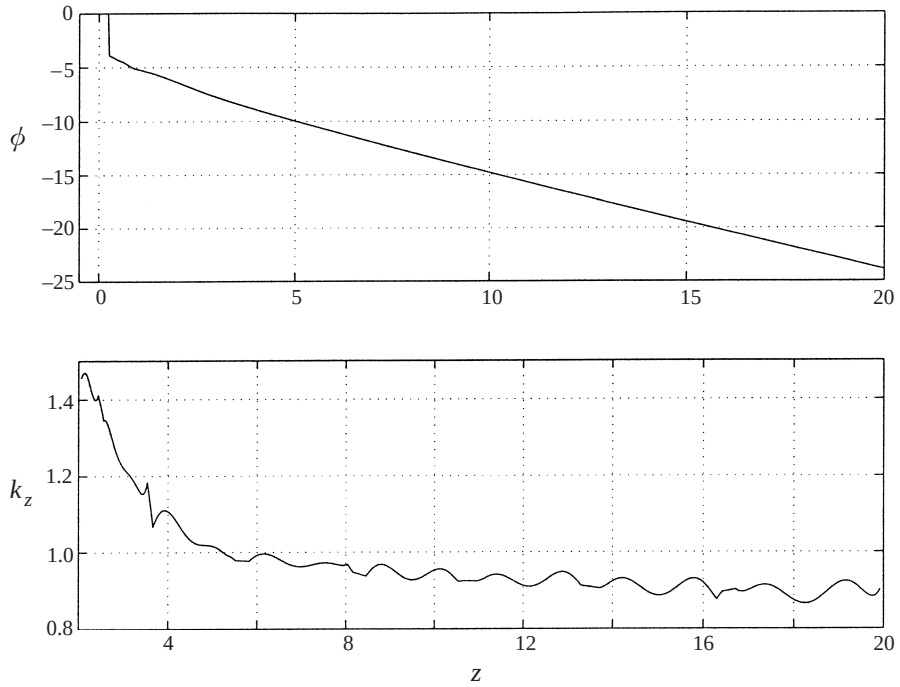

FIGURE 21. Axial variation of (*a*) the phase ϕ and (*b*) the wavenumber k_z for the mode $n = 1$, $m = 1$ at $r = 0.46$.

find a wavelength of 6 or less in this region (see Ormières (1999) or vorticity plots of Johnson & Patel (1999)).

Dušek (1996) points out that the asymptotic wavenumber of higher time Fourier modes is exactly proportional to the order of the mode, which means that higher-order harmonics have the same asymptotic phase velocity as the fundamental mode. This is also the case for the sphere wake. For example, the second harmonic $n = 2$ of the axial component of the $m = 1$ mode has an asymptotic wavenumber of quite accurately $k_z = 1.8$ i.e. twice the wavenumber of the fundamental mode. This means that the asymptotic phase velocity has the same value for all modes. Taking account of the angular frequency of the fundamental mode $\omega = 0.8389$ and of its asymptotic wavenumber $k_z = 0.9$, the asymptotic phase velocity is about 0.9 (90% of the inflow velocity) which is practically the same as for the infinite cylinder wake (Williamson 1989).

The double Fourier mode decomposition is a good characterization of the limit cycle because it allows most of the features observed experimentally or simulated numerically in the un-decomposed flow field to be reproduced very easily. Moreover, due to a very rapid convergence of the expansion it provides the essential information condensed in a very restricted number of two-dimensional modes, typically six in the Reynolds number range investigated ($m = 0, 1, 2$ and $n = 0, 1$).

7. Conclusions

The discretization combining spectral elements with a spectral azimuthal expansion proves to be a tool well adapted to simulation of instabilities arising in axisymmetric geometries if submitted to thorough optimization and accuracy control. It allows

the computing costs of the sphere wake simulation to be reduced to reasonable levels while providing a very satisfactory accuracy. The azimuthal expansion at the primary, symmetry-breaking instability, and the time Fourier expansion at the secondary one have been shown to be directly related to the nonlinear instability theory, which explains their practical interest. They provide a very useful analysis of the flow field allowing an explanation of some so far not quite understood phenomena. In the steady non-axisymmetric regime it was possible to explain the origin of the so-called bifid wake and predict its presence at all Reynolds numbers. In the unsteady periodic regime, a very reduced number of modes allows the flow dynamics to be characterized accurately. For both regimes, the accuracy tests provided useful information concerning the instability thresholds. Comparison with previous experimental and numerical data is shown to be an easy matter and the agreement, especially with the meticulous experiments of Ormières (1999), is very satisfactory.

From the theoretical point of view, the primary instability was fully analysed as an axisymmetry-breaking instability generalizing the behaviour at a pitchfork bifurcation to the case of a continuous symmetry group. It was shown that the axisymmetry gives way to plane symmetry, the orientation of the symmetry plane being random (i.e. determined only by the initial conditions) if the original axisymmetry is perfect and in the absence of any external perturbation. The theory of axisymmetry breaking by a regular bifurcation is analogous to that of the time-invariance breaking at a Hopf bifurcation, the time invariance being replaced by the rotational one. Conclusions concerning the mode amplification and instability saturation drawn in Dušek (1996) and Carte *et al.* (1996) for Hopf bifurcations can be directly applied.

The secondary instability presents the same typical features of Hopf bifurcations already found to characterize the cylinder wake. Close to the instability threshold the weakly nonlinear Landau model is shown to hold with a good accuracy and the missing value of the normalized Landau constant could be determined.

The investigations can be pushed further to higher Reynolds numbers. Simulations of Tomboulides *et al.* (1993) and preliminary tests of the code presented prove the possibility of investigating the whole transition to turbulence. Regarding the third bifurcation setting in at about $Re = 360$ to 375 (Ormières 1999; Mittal 1999*b*) there are two important questions to be elucidated. The first is whether the observed plane-symmetry breakup is an intrinsic symmetry breaking or is due to the weak stability of the attractor and its sensitivity to helical perturbation; the second one is whether the attractor that arises is a true limit torus or a more complicated limit cycle. The investigation of further transition stages needs special caution and might be a costly task requiring high accuracy and thorough numerical tests if intrinsic dynamics is to be reliably distinguished from numerical artifacts.

The work was partly supported by the Réseau Formation/Recherche "Europe Centrale et Orientale" of the French Ministry of Education.

Appendix

A.1. *Resolved system of equations*

The system of azimuthal modes $\boldsymbol{v}_m, p_m$ satisfies (2.17) with $\Lambda_{|m|}[\boldsymbol{V}] = \Lambda_{|m|}[0]$, i.e. with $\boldsymbol{V}$ replaced by zero in the expression for the linear operator (2.10). Even with $\boldsymbol{V} = 0$ the linear operator (2.10) couples the radial v_m and azimuthal w_m components. Following Orszag (1974) it is possible to obtain a decoupled system of equations

using the following change of variables:

$$\tilde{v}_m = v_m - \mathrm{sgn}(m) w_m, \tag{A 1a}$$

$$\tilde{w}_m = v_m + \mathrm{sgn}(m) w_m. \tag{A 1b}$$

Placing (A 1*a*) and (A 1*b*) in equations (2.17) we arrive at the system

$$\frac{\partial u_m}{\partial t} + \mathscr{F}_{m,z} = -\frac{\partial p_m}{\partial z} + \nu \nabla^2_{m^2} u_m, \tag{A 2a}$$

$$\frac{\partial \tilde{v}_m}{\partial t} + \mathscr{F}_{m,r} = -\left(\frac{\partial p_m}{\partial r} - m\frac{p_m}{r}\right) + \nu \nabla^2_{(m+1)^2} \tilde{v}_m, \tag{A 2b}$$

$$\frac{\partial \tilde{w}_m}{\partial t} + \mathscr{F}_{m,\theta} = -\left(\frac{\partial p_m}{\partial r} + m\frac{p_m}{r}\right) + \nu \nabla^2_{(m-1)^2} \tilde{w}_m, \tag{A 2c}$$

$$\tilde{\boldsymbol{\nabla}}^{\dagger}_m \cdot \tilde{\boldsymbol{v}}_m = 0, \tag{A 2d}$$

with the divergence operator $\tilde{\boldsymbol{\nabla}}^{\dagger}_m$ defined as

$$-\tilde{\boldsymbol{\nabla}}^{\dagger}_m = \left(\frac{\partial}{\partial z}, \frac{1}{2}\left(\frac{1}{r}\frac{\partial}{\partial r}(r\bullet) + \frac{m}{r}\right), \frac{1}{2}\left(\frac{1}{r}\frac{\partial}{\partial r}(r\bullet) - \frac{m}{r}\right)\right), \tag{A 3}$$

and with

$$\boldsymbol{v}_m = (u_m, v_m, w_m), \quad \tilde{\boldsymbol{v}}_m = (u_m, \tilde{v}_m, \tilde{w}_m). \tag{A 4a,b}$$

It is important to remark that while $\bar{\boldsymbol{v}}_m = \boldsymbol{v}_{-m}$, $\bar{\tilde{v}}_m = \tilde{w}_{-m}$. The nonlinear terms are written in a compact way as $\mathscr{F}_{m,z}, \mathscr{F}_{m,r}, \mathscr{F}_{m,\theta}$ and are given below.

We note that the gradient is represented by the operator

$$\tilde{\boldsymbol{\nabla}}_m = \left(\frac{\partial}{\partial z}, \left(\frac{\partial}{\partial r} - m\frac{1}{r}\right), \left(\frac{\partial}{\partial r} + m\frac{1}{r}\right)\right)^T \tag{A 5}$$

and that the divergence operator is adjoint to $-\tilde{\boldsymbol{\nabla}}_m$ (whence the superscript † in (A 3)). As a result

$$-\tilde{\boldsymbol{\nabla}}^{\dagger}_m \cdot \tilde{\boldsymbol{\nabla}}_m = \nabla^2_{m^2}. \tag{A 6}$$

For the time integration of the equation system (A 2) we use a classical splitting method (Ronquist 1988). The spatial discretization of (A 2) is performed using the spectral element method (Patera 1984). The computational domain Ω is broken up into general quadrilaterals, which are mapped isoparametrically to canonical squares (Karniadakis & Triantafyllou 1992). In the subdomains away from the axis, the expansion of the solution is performed using standard Legendre–Lagrangian interpolants based on Gauss–Legendre–Lobatto points.

For the elements close to the axis, the presence of singular factors $1/r$ and $1/r^2$ in the governing equations (A 2) demands a special treatment. In order to deal with these terms one can take advantage of the physical requirement that the flow has a single value at $r = 0$. This condition implies that all azimuthal modes are zero at the flow axis except u_0, p_0, $\tilde{v}_{-1}$ and $\tilde{w}_1$, which shows that the singularities are removable. The weight factor r appearing in the weak formulation of the spectral-element discretization is accounted for by using Jacobi collocation points in elements adjacent to the axis (Ronquist 1988).

In Tomboulides *et al.* (1993) the nonlinear terms are evaluated in the physical space and then transformed, by a FFT, to the azimuthal Fourier space for the linear part of the calculation. This technique is efficient if a significant number of azimuthal

	Fornberg (1988)	Johnson & Patel (1999)	Present paper
Recirculation length	1.935	1.945	1.940
Detachment angle	–	61°	62.2°

TABLE 6. Comparison of the recirculation length and of the detachment angle to values from other work at $Re = 200$. The full mesh with 6 collocation points is used.

modes is to be computed (32 in Tomboulides *et al.* 1993). In this paper, a very small number of azimuthal modes yields a very good accuracy in the investigated Reynolds number domain. Tests show that the maximal number of modes necessary to correctly approximate the flow for Reynolds numbers less than 300 is only five. We therefore calculate directly the truncated convolution of nonlinear terms in Fourier space. If only a finite number of azimuthal modes $(\boldsymbol{v}_0, \cdots, \boldsymbol{v}_{M_{max}})$ is taken to describe the flow the nonlinear terms are reduced to finite sums:
axial:

$$\begin{aligned}\mathscr{F}_{m,z} = \sum_{k=-\infty}^{+\infty} (\sigma(k)\boldsymbol{v}_k \cdot \nabla_{m-k})\, u_{m-k} \approx \sum_{k=1}^{M_{max}-m} \left(\overline{\sigma(k)\boldsymbol{v}_k} \cdot \nabla_{m+k}\right) u_{m+k} \\ + \sum_{k=0}^{m} (\sigma(k)\boldsymbol{v}_k \cdot \nabla_{m-k})\, u_{m-k} + \sum_{k=m+1}^{M_{max}} (\sigma(k)\boldsymbol{v}_k \cdot \nabla_{m-k})\, \bar{u}_{k-m}, \\ m = 0, \ldots, M_{max}, \end{aligned} \tag{A 7a}$$

radial:

$$\begin{aligned}\mathscr{F}_{m,r} = \sum_{k=-\infty}^{+\infty} (\sigma(k)\boldsymbol{v}_k \cdot \nabla_{m-k+1})\, \tilde{v}_{m-k} \approx \sum_{k=1}^{M_{max}-m} \left(\overline{\sigma(k)\boldsymbol{v}_k} \cdot \nabla_{m+k+1}\right) \tilde{v}_{m+k} \\ + \sum_{k=0}^{m} (\sigma(k)\boldsymbol{v}_k \cdot \nabla_{m-k+1})\, \tilde{v}_{m-k} + \sum_{k=m+1}^{M_{max}} (\sigma(k)\boldsymbol{v}_k \cdot \nabla_{m-k+1})\, \bar{\tilde{w}}_{k-m}, \\ m = 0, \ldots, M_{max}, \end{aligned} \tag{A 7b}$$

azimuthal:

$$\begin{aligned}\mathscr{F}_{m,\theta} = \sum_{k=-\infty}^{+\infty} (\sigma(k)\boldsymbol{v}_k \cdot \nabla_{m-k-1})\, \tilde{w}_{m-k} \approx \sum_{k=1}^{M_{max}-m} \left(\overline{\sigma(k)\boldsymbol{v}_k} \cdot \nabla_{m+k-1}\right) \tilde{w}_{m+k} \\ + \sum_{k=0}^{m} (\sigma(k)\boldsymbol{v}_k \cdot \nabla_{m-k-1})\, \tilde{w}_{m-k} + \sum_{k=m+1}^{M_{max}} (\sigma(k)\boldsymbol{v}_k \cdot \nabla_{m-k-1})\, \bar{\tilde{v}}_{k-m}, \\ m = 0, \ldots, M_{max}, \end{aligned} \tag{A 7c}$$

where ∇_m is the operator (2.19).

A.2. *Results of numerical tests*

Numerical tests of the spectral-element decomposition consisted partly in reproducing the known results of Fornberg (1988) and of Johnson & Patel (1999) concerning the recirculation length and the detachment angle (see table 6).

The ultimate test criterion was, however, the mesh independence of the primary

	Basic domain	Upstream extent	Downstream extent	Spanwise extension	Whole domain
λ	0.0146	0.0115	0.0131	0.0133	0.0119
ΔRe	–	−1.0	−0.5	−0.4	−0.9

TABLE 7. Amplification rates for different domain extensions and equivalent Reynolds number variation with respect to the basic domain.

$Re = 215$	$N = 6$	$N = 8$	$N = 10$	$N \to \infty$ (estimation)
λ	0.0119	0.0098	0.0088	0.0079

TABLE 8. Dependence of the amplification rate on the number of collocation points.

unstable eigenvalue of the linearized eigenvalue problem (2.9*b*). This eigenvalue gives the non-dimensionalized amplification rate of the instability (i.e. the amplification rate expressed in units based on the cylinder diameter and asymptotic flow velocity). The resolved system (A 2) reduces to an eigenvalue problem by truncation to the modes $m = 0, 1$ and by switching off the coupling with the $m = 1$ mode in the $m = 0$ equation. As a result, the computation of the base flow is decoupled (and reduces to the axisymmetric computation). As soon as the base flow is obtained, it is input to the $m = 1$ equation yielding the unstable $m = 1$ mode. This computation was first carried out in the 'basic' domain defined in the caption of figure 3 obtained by cutting off one layer of elements in the upstream, downstream and radial directions. The resulting amplification rates are assembled in table 7. In table 9 we give the dependence of the amplification rate on the Reynolds number. It allows us to conclude that an increase of the Reynolds number by 1 corresponds roughly to an increase of the amplification by 0.003. On this basis we can relate the amplification rate variations in table 7 to the Reynolds number variations. We can conclude that the overall effect of extending the basic domain to the full one given in figure 3 represents at most an amplification rate variation corresponding roughly to a Reynolds number variation by 1. The use of the large domain guarantees that further increase of its diameter or length would have insignificant effects on the relation between the Reynolds number and the amplification rates.

A progressive increase of the number of collocation points corresponds to an increase of the number of elements of the pseudospectral expansion and is expected to yield an exponential convergence (Patera 1984). For $N = 6, 8, 10$, N being the number of collocation points per spatial direction ($N = 6$ means a total number of 36 collocation points in the two-dimensional element), we computed, again at $Re = 215$, the amplification rates on the whole computational domain represented in figure 3. On the basis of the assumption of exponential convergence the extrapolated 'exact' value resulting from table 8 would lie approximately 4×10^{-3} lower than the value obtained for $N = 6$. The significantly higher computing costs necessary to run the computation with a higher number of collocation points do not to seem to be justified. The systematic decrease of the amplification rate with increasing accuracy allows us to assert that the amplification rates are systematically overpredicted and thus the critical Reynolds number is expected to be underpredicted by about 1.4. The eigenvalue has first been computed for $Re = 200$ and $Re = 215$, an estimate of the

	$Re = 200$	$Re = 210$	$Re = 211$	$Re = 215$
λ	-0.0353	-0.0019	6.1×10^{-4}	0.0119

TABLE 9. Amplification rates for different Re using the full computational domain and $N = 6$ resulting in a critical Re of $Re_1 \approx 210.8$.

critical Reynolds number yielding a value between 210 and 211 has been obtained by linear interpolation and, finally, a more accurate value is given by the eigenvalue obtained at $Re = 210$ and $Re = 211$ (see table 8). Interpolation between the values obtained at $Re = 210$ and $Re = 211$ yields $Re_1 = 210.8$. Taking account of the underprediction estimated above, the likely accurate value of the critical Reynolds number lies at $Re_1 \approx 212.2$.

A.3. *Computing costs*

On DEC XP600 and XP1000 machines the simulation of a period of oscillations at $Re = 300$ took, respectively 2 and 1 hour with the azimuthal expansion truncated at the 6th mode and with the spectral-element discretization specified in § 4. This time is easily reduced by a factor of two if only three azimuthal modes are used without sacrificing much precision. Another issue is to find a minimal numerical model that allows one to capture the dynamics at least qualitatively. For this purpose, we reduced the mesh without worrying about the accuracy, the only concern being to keep the numerical stability (the spectral-element code tends to diverge if not enough resolution is provided). A 32 spectral element mesh extending $8d$ upstream, $18d$ downstream and $4.5d$ in the radial direction appeared to be sufficient to provide a numerically stable solution at $Re = 300$. Special care needs to be given to zones with steep velocity gradients in the near wake where the interpolation polynomials risk bringing about destabilizing oscillations. Otherwise, even a smaller domain would present an acceptable dynamics. Two modes $m = 0$ and $m = 1$ are sufficient to provide a periodic solution at $Re = 300$. The Strouhal number is overpredicted ($St = 0.16$) and also the oscillation amplitude is about 25% higher than the correct value corresponding to the given Reynolds number. This is not surprising given the tendency of the code to enhance instabilities with low resolution. This quantitative disagreement may sometimes not be a nuisance while the computing costs are divided by a factor of about 30 (2 to 4 minutes per oscillation period).

REFERENCES

ACHENBACH, E. 1974 Vortex shedding from spheres. *J. Fluid Mech.* **62**, 209–221.

CARTE, G., DUŠEK, J. & FRAUNIÉ, PH. 1996 Numerical simulation of the mechanisms governing the onset of the Bénard–von Kármán instability. *Intl J. Numer. Meth. Fluids* **23**, 753–785.

DĂNĂILĂ, I., DUŠEK, J. & ANSELMET, F. 1997 Coherent structures in a round, spatially evolving, unforced, homogeneous jet at low Reynolds numbers. *Phys. Fluids* **9**, 3323–3342.

DĂNĂILĂ, I., DUŠEK, J. & ANSELMET, F. 1998 Complex dynamics at a Hopf bifurcation with axisymmetry breaking in a jet. *Phys. Rev.* E **57**, 3695–3698.

DAUCHY, CH., DUŠEK, J. & FRAUNIÉ, PH. 1997 Primary and secondary instabilities in the wake of a cylinder with free ends. *J. Fluid Mech.* **332**, 295–339.

DUŠEK, J. 1996 Spatial structure of the Bénard–von Kármán instability. *Eur. J. Mech.* B/*Fluids* **15**, 619–650.

DUŠEK, J., FRAUNIÉ, PH. & LE GAL, P. 1994*a* Local analysis of the onset of instability in shear flows. *Phys. Fluids* **6**, 172–186.

Dušek, J., Le Gal, P. & Fraunié, Ph. 1994*b* A numerical and theoretical study of the first Hopf bifurcation in a cylinder wake. *J. Fluid Mech.* **264**, 59–80.

Fornberg, B. 1988 Steady viscous flow past a sphere at high Reynolds numbers. *J. Fluid Mech.* **190**, 471–489.

Goldburg, A. & Florsheim, B. H. 1966 Transition and Strouhal number for the incompressible wake of various bodies. *Phys. Fluids* **9**, 45–50.

Jackson, C. P. 1987 A finite-element study of the onset of vortex shedding in flow past variously shaped bodies. *J. Fluid Mech.* **182**, 23–45.

Jeong, J. & Hussain, F. 1995 On the identification of a vortex. *J. Fluid Mech.* **285**, 69–94.

Johnson, T. A. & Patel, V. C. 1999 Flow past a sphere up to a Reynolds number of 300. *J. Fluid Mech.* **378**, 19–70.

Karniadakis, G. E. & Triantafyllou, G. S. 1992 Three-dimensional dynamics and transition to turbulence in the wake of bluff objects. *J. Fluid Mech.* **238**, 1–30.

Kim, I. & Pearlstein, A. J. 1990 Stability of the flow past a sphere. *J. Fluid Mech.* **211**, 73–93.

Levi, E. 1980 Three-dimensional wakes: origin and evolution *J. Engng Mech. Div.* **EM4**, 659–676.

Magarvey, R. H. & Bishop, R. L. 1961*a* Transition ranges for three-dimensional wakes. *Can. J. Phys.* **39**, 1418–1422.

Magarvey, R. H. & Bishop, R. L. 1961*b* Wakes in liquid–liquid systems. *Phys. Fluids* **4**, 800–805.

Magarvey, R. H. & MacLatchy, C. S. 1965 Vortices in sphere wakes. *Can. J. Phys.* **43**, 1649–1656.

Michalke, A. 1984 Survey on jet instability theory. *Prog. Aerospace Sci.* **21**, 159–199.

Mittal, R. 1999*a* A Fourier Chebyshev spectral collocation method for simulating flow past spheres and spheroids. *Intl J. Numer. Meth. Fluids* **30**, 921–937.

Mittal, R. 1999*b* Planar symmetry in the unsteady wake of a sphere. *AIAA J.* **37**, Technical Notes, 388–390.

Monkewitz, P. A. 1988 A note on vortex shedding from axisymmetric bluff bodies. *J. Fluid Mech.* **192**, 561–575.

Nakamura, I. 1976 Steady wake behind a sphere. *Phys. Fluids* **19**, 5–8.

Natarajan, R. & Acrivos, A. 1993 The instability of the steady flow past spheres and disks. *J. Fluid Mech.* **254**, 323–344.

Ormières, D. 1999 Etude expérimentale et modélisation du sillage d'une sphère à bas nombre de Reynolds. PhD Thesis, Université de Provence.

Ormières, D. & Provansal, M. 1999 Transition to turbulence in the wake of a sphere. *Phys. Rev. Lett.* **83**, 80–83.

Orszag, S. A. 1974 Fourier series on spheres. *Mon. Weath. Rev.* **102**, 56.

Patera, A. T. 1984 A spectra element method for fluid dynamics; laminar flow in a channel expansion. *J. Comput. Phys.* **54**, 468.

Provansal, M. & Ormières, D. 1997*a* Transition to turbulence in the wake of axisymmetric objects. *11th Symposium on Turbulent Shear Flow, Grenoble.*

Provansal, M. & Ormières, D. 1997*b* Visualisation de sillages de sphère, cône et de disque. *Visu 97* (ed. P. Smigielski), pp. 147–152. Teknea, Saint Louis.

Provansal, M. & Ormières, D. 1998 Étude expérimentale de l'instabilité du sillage d'une sphère. *C. R. Acad. Sci. Paris* **326**, II b, 489–494.

Ronquist, E. M. 1988 Optimal spectral element methods for the unsteady three-dimensional incompressible Navier–Stokes equations. *PhD Thesis, Massachusetts Institute of Technology.*

Sakamoto, H. & Haniu, H. 1990 A study on vortex shedding from spheres in a uniform flow. *Trans. ASME* I: *J. Fluids Engng* **112**, 386–392.

Sakamoto, H. & Haniu, H. 1995 The formation mechanism and shedding frequency of vortices from a sphere in uniform shear flow. *J. Fluid Mech.* **287**, 151–171.

Sreenivasan, K. R., Strykowski, P. J. & Olinger, D. J. 1987 Hopf bifurcation, Landau equation and vortex shedding behind circular cylinders. *Proc. Forum on Unsteady Flow Separation, ASME Applied Mechanics, Bio Engineering and Fluid Engineering Conference, Cincinnati, Ohio, June 11–17, 1987.* ASME FED, Vol. 52.

Strogatz, S. H. 1994 *Nonlinear Dynamics and Chaos*, pp. 55, 56. Addison Wesley.

Tomboulides, A. G., Orszag, S. A. & Karniadakis, G. E. 1993 Direct and large-eddy simulation of axisymmetric wakes. *AIAA Paper* 93-05-6.

WILLIAMSON, C. H. K. 1989 Oblique and parallel modes of vortex shedding in the wake of a circular cylinder at low Reynolds numbers. *J. Fluid Mech.* **206**, 579–627.

WILLMARTH, W. W., HAWK, N. E. & HARVEY, R. L. 1964 Steady and unsteady motions and wakes of freely falling disks. *Phys. Fluids* **7**, 197–208.

ZIELINSKA, B. J. A., GOUJON-DURAND, S., DUŠEK, J. & WESFREID, J. E. 1997 A strongly nonlinear effect in unstable wakes. *Phys. Rev. Lett.* **79**, 3893–3896.